Estimating the masses of z > 2.5 quasars from accretion disk models

A thesis presented
by
Alex Krolewski

Submitted to

The Department of Astronomy

in partial fulfilment of the requirements

for the degree of Bachelor of Arts

Thesis advisor: Aneta Siemiginowska

April 11, 2014

ABSTRACT

Black hole masses for $z > 2$ quasars are typically estimated from single-epoch spectroscopy using the monochromatic continuum luminosity at 1350 Å and the CIV 1549 Å line width. These masses exhibit large scatter (≈ 0.5 decades) from the true masses and are subject to large systematic errors due to the idiosyncrasies of the CIV line profile. As a result, in this thesis I estimate the masses of a sample of 86 $z > 2.5$ radio-loud quasars by fitting accretion disk models to the restframe ultraviolet quasar spectra. I also fit accretion disk models to a matched sample of 86 radio-quiet quasars, in order to both explore the differences between radio loud and radio quiet quasars and estimate the possible contribution from strong radio jets or synchrotron emission to the radio-loud quasar continuum. Finally, I explore the errors introduced by several different systematic effects and give a rough accounting of the total error budget of the mass estimates.

Acknowledgements

I would like to acknowledge the assistance and support of many people on this project, and generally throughout my astronomy career at Harvard. First and most importantly, I would like to thank my advisor, Aneta Siemiginowska, for providing the motivation behind my thesis and for her support throughout the project. From her I have learned a tremendous amount about quasars! I would also like to thank my Astro 98 advisor, Daniel Eisenstein, for initially introducing me to the world of quasar research, and ultimately sparking my interest in determining quasar masses. I would also like to thank Research Computing at Harvard and those who run the Odyssey cluster, without which none of my project would have happened. I would also like to acknowledge Charles Alcock for leading the Astro 99 class, and my fellow thesis writers for persevering and creating a supportive environment. Going further back, I would like to thank David Charbonneau for piquing my

interest in astronomy with his boundless enthusiasm in Astronomy 16. Finally, I would like to thank my family and friends for their support throughout college!

Contents

1. Background

1.1. Historical overview: quasars are powered by accretion disks

Quasars are the most luminous objects in the universe, with luminosities up to 1000 times greater than a typical ($L_\star$) galaxy (Krolik 1999). Quasars are also tiny: the nucleus of a quasar has never been optically resolved, and must be less than 1 pc across. The most likely possibility for such an incredible luminosity and small size is an accretion disk around a supermassive ($10^8 M_\odot$) black hole (Rees 1984). As gas falls into the deep gravitational potential well of the black hole, its gravitational energy is converted into kinetic energy and radiated as light due to friction in the disk. This process is considerably more efficient at converting energy to electromagnetic radiation than nuclear fusion, with an efficiency (energy released divided by rest mass) of approximately 0.1, compared to an efficiency of 10^{-3} for nuclear fusion (Krolik 1999).

In addition to their exceptional luminosity and tiny size, quasars' rest-frame optical and UV spectra exhibit very strong, broad emission lines, implying velocities up to ≈ 10000 km s^{-1}, and quasars are very bright across the entire electromagnetic spectrum, from radio to X-ray. Quasars are divided into many subclasses based on their emission line properties and flux at different frequencies. Type 1 quasars exhibit both the characteristic broad lines as well as much narrower lines in the optical and ultraviolet, while type 2 quasars exhibit only the narrow lines. The broad lines arise exclusively from permitted or semiforbidden transitions, while the narrow lines arise only from forbidden transitions. As a result, the broad and narrow lines are believed to arise from physically distinct regions: the broad lines come from dense gas in the broad line region located just beyond the edge of the accretion disk, while the narrow lines come from diffuse gas in the host galaxy lit by the continuum source (Krolik 1999). It is believed that type 1 and type 2 quasars are physically identical, and that the broad line region in type 2 quasars is obscured by a torus of hot dust very close to the supermassive black hole (Urry & Padovani 1995).

Quasars are often also subdivided based on their radio emission properties. About 15-20% of quasars are radio loud, with $R \equiv F_\nu(5\text{ GHz})/F_\nu(4400\text{ Å}) > 30$, while the remaining 80-85% of quasars are radio quiet. There are few quasars with intermediate radio properties: the radio flux distribution is quite bimodal (Krolik 1999). Additional subdivisions of radio-loud quasars are determined by the quasar's radio properties, including FR1 and FR2 quasars and BL Lac objects (also known as blazars), which lack emission and absorption lines and are strongly variable and polarized.

The broad spectrum observed in quasars arises from several different sources. Radio emission in radio loud quasars is synchrotron radiation from highly relativistic charged particles spiraling through magnetic fields near the supermassive black hole. In blazars, synchrotron radiation dominates the quasar's bolometric luminosity and is therefore responsible for the rest-frame optical and ultraviolet emission, explaining the strong optical variability and polarization. In other types of quasars, radiation in the optical and ultraviolet is dominated by thermal emission from the accretion disk itself, while emission from the host galaxy is also significant in the optical and near-infrared, particularly for lower luminosity or Type 2 quasars. Quasars also exhibit an infrared bump consisting of emission from hot dust in the torus surrounding the black hole; the dust absorbs incident optical and ultraviolet light from the accretion disk and reradiates it in the infrared. Last, quasars emit X-rays, which most likely result from reprocessing of lower-energy emission from the accretion disk, likely via bremsstrahlung or inverse Compton scattering. One notable component of the X-ray spectrum with an unknown source is the "soft excess," consisting of a bump at energies below 1 keV. The shape of the soft excess is not well-established and the strength varies from object to object (Krolik 1999).

Soon after accretion was identified as the source of quasars' prodigious emission, Shakura & Sunyaev (1973) determined the equations governing accretion in a geometrically thin, optically thick disk. They suggested that the resulting spectrum is a multi-temperature blackbody: if the disk is optically thick and has negligible spatial extent, the spectrum

at each annulus is a blackbody with the temperature set by the total flux using the Stefan-Boltzmann law. For a 10^8 $M_\odot$ black hole, Shakura & Sunyaev (1973) predicted that the spectrum would peak in the ultraviolet. Shields (1978) first identified the thermal accretion disk spectrum with the "big blue bump" peaking near 1000 Å.

While the simple multi-temperature blackbody model successfully predicts the existence of the big blue bump, it has several theoretical failings: it neglects the vertical structure of the disk; it assumes the disk emits as a blackbody; it neglects general relativistic corrections to the angular velocity; and it assumes the black hole is not spinning. Several extensions to the Shakura & Sunyaev (1973) model relax these assumptions: the blackbody emission is replaced by a color-temperature corrected blackbody to roughly approximate the spectral hardening caused by inverse Compton scattering; the potential is modified to empirically correct for general relativistic effects and a zero-torque inner boundary condition is imposed (the DISKPN model of Gierliński et al. 1999); full general relativistic corrections are taken into account and the black hole is allowed to rotate (the KERRBB model of Li et al. 2005); a hot corona in the inner part of the disk is added to account for the soft excess (Done et al. 2012). More sophisticated extensions consist of modeling the full radiative transfer within the disk and are substantially more complex than the Shakura & Sunyaev (1973) model or its simple extensions (Hubeny et al. 2000; Slone & Netzer 2012; Laor & Davis 2014).

Nevertheless, even the most sophisticated accretion disk models are not entirely consistent with observations. Using nearly-simultaneous spectroscopy from three different instruments spanning 900-9000 Å in rest-frame wavelength, Shang et al. (2005) find a rough agreement between the UV-optical and far-UV spectral slopes of 17 quasars and the Hubeny et al. (2000) thin accretion disk model. However, they find that the data do not reproduce the relationship between black hole mass and far UV slope predicted by the Hubeny et al. (2000) model, although they note that this discrepancy can be explained by modest intrinsic dust reddening ($E(B-V) = 0.04$) or Compton scattering converting a significant fraction of the disk flux to extreme UV or X-ray emission. Davis et al. (2007) measure the 2200–4000

Å and 1450–2200 Å spectral slopes for ≈ 3000 quasars from SDSS and compare these slopes to predictions from the Hubeny et al. (2000) model. Similar to Shang et al. (2005), they find that the observed slopes depend only weakly on black hole mass and luminosity, whereas the modelled slopes are much stronger functions of mass and luminosity. Davis et al. (2007) find that this discrepancy may be explained by modest intrinsic reddening ($E(B-V) < 0.03$) and/or considerably larger errors in the mass estimates than commonly assumed. More encouragingly, Capellupo et al. (2015) satisfactorily fit the thin accretion disk model of Slone & Netzer (2012) to 22 of 30 quasars observed from rest-frame 1200 to 9800 Å using *X-shooter* on the VLT. The discrepancies between the model and most of the remaining 8 quasars can be explained by either intrinsic reddening or disk winds, which are not included in the Slone & Netzer (2012) model. The Capellupo et al. (2015) result is a more sensitive test of the thin disk models that either the results of Shang et al. (2005) or Davis et al. (2007): Capellupo et al. (2015) considers a much larger wavelength range using data from a single instrument, eliminating scatter arising from source variability or differing calibrations between instruments. Moreover, Capellupo et al. (2015) fit the accretion disk models to the spectra rather than relying on the models' predicted spectral slopes. Taken together, these results indicate that while there are significant difficulties and uncertainties involved in the model fitting, thermal emission from thin accretion disks is responsible for the optical and ultraviolet quasar continuum.

In this paper we use the DISKPN model with a color-temperature correction rather than one of its more complicated cousins. The difficulties in fitting the more complicated accretion disk models suggest that the drastically increased complexity and computational costs of the more complicated models may outweigh the gains in accuracy. Nevertheless, we will carefully consider the differences between the more complicated models and the DISKPN model in order to assess the model-dependence of our results.

1.2. Black hole mass estimation

Measuring the mass of the central supermassive black hole gives insight into the physical conditions of the quasar. The most reliable mass estimates for black holes in quiescent galaxies come from direct dynamical detection, using spatially resolved spectroscopy to directly measure the velocity of the gas very close to the black hole (see Kormendy & Ho 2013, for a review). However, the strength of emission from the central black hole makes this method challenging to implement for quasars. Instead, most quasar mass estimates are based on the assumption that gas in the broad-line region is virialized, with its motion fully determined by the potential of the central black hole. If both the velocity and the radius of the gas are known, then the mass can be determined:

$$M = f\frac{w^2 r}{G} \tag{1}$$

where w is a measurement of line width (either the FWHM or the line dispersion σ) and f is a factor relating the line width to the velocity. The broad-line region radius can be estimated using reverberation mapping: as the continuum flux changes, the flux of the broad lines follows, but its response is lagged with a time delay proportional to the distance between the broad line region and the central black hole (Blandford & McKee 1982). The resulting masses (Wandel et al. 1999; Vestergaard & Peterson 2006) are generally considered the most accurate available masses for supermassive black holes in quasars (Shen 2013). However, since reverberation mapping requires extensive multi-epoch spectroscopy and some variability in the quasar emission, it is not well suited to large samples of quasars or high-redshift quasars, where the time delay is redshifted by a factor of $1 + z$. In order to estimate masses for large samples of quasars, a method using only single-epoch spectroscopy has been developed, based on the finding that the optical luminosity and radius are tightly related with little scatter: $R \propto L^{0.5}$ or $R \propto L^{0.62}$ (Kaspi et al. 2000; Bentz et al. 2009). This relationship is physically motivated by photoionization arguments: the broad-line region requires an ionizing source, and therefore its size is regulated by the amount of ionizing radiation emitted by the central black hole. Since the ionizing UV radiation is correlated

with the optical emission, the optical emission is related to the broad line region size. Thus, the single-epoch mass is given by the following relationship:

$$\log M = a + b \log L + c \log W \tag{2}$$

where W is the line width and L is the monochromatic continuum luminosity. The coefficients a and b are calibrated to reverberation mapping masses, while c is typically fixed at 2. If only optical spectra are available (as for large surveys such as the Sloan Digital Sky Survey), the line and monochromatic luminosity used to estimate the mass are dictated by the redshift: Hβ and L_{5100} for $z < 0.7$, MgII and L_{3000} for $0.7 < z < 2$, and CIV and L_{1350} for $z > 2$. Since the reverberation-mapped sample only extends to $z \approx 0.3$, the calibrations in Equation 2 are most certain for low-redshift quasars.

The statistical errors on both the reverberation-mapping masses and the single epoch masses are $\approx$ 0.3-0.5 dex (Shen 2013; Vestergaard & Peterson 2006). More concerning are possible systematic errors in the mass estimates. One source of systematic error is the virial coefficient f. Since f relates the line width to the virial velocity, it should vary from source to source with the cosecant of the BLR inclination angle. However, since the inclination angle cannot be measured for individual sources, an average value of f is used for all quasars. While f can be calculated from first principles by considering the range of possible orientations and line profiles, in practice f is generally estimated by assuming that the normalization of the $M_{\rm BH} - \sigma$ relationship is the same for quasars as for local quiescent galaxies (Onken et al. 2004; Woo et al. 2010). This assumption may not be true, and in addition, the normalization of the $M_{\rm BH} - \sigma$ relationship depends on the type of galaxy analyzed, leading to a systematic uncertainty in the determination of f (Shen 2013).

Another source of systematic error is the assumption that the line width arises entirely from virial motion. If this assumption is correct, then changes in line width should be compensated by anticorrelated changes in BLR radius or optical luminosity, ensuring that the mass remains constant. For reverberation-mapping masses, changes in BLR radius are indeed anticorrelated with changes in CIV and Hβ line widths (Peterson et al. 2004).

However, the evidence is more mixed for the single-epoch masses: variations in Hβ line width are anticorrelated with variations in continuum luminosity, but changes in MgII and CIV line widths are not correlated with variations in continuum luminosity for more luminous, higher-redshift quasars (see Figure 1 in Shen 2013; Wilhite et al. 2007). As a result, Wilhite et al. (2007) finds a 1 σ error of 0.3 decades in CIV masses arising solely from variability between different epochs.

Comparing Hβ, MgII, and CIV masses for the same object provides another test of the accuracy of the virial masses. Reverberation mapping masses for Hβ are consistent with CIV-based masses (Vestergaard & Peterson 2006). However, single-epoch Hβ masses generally do not agree well with single-epoch CIV masses (Baskin & Laor 2005; Netzer et al. 2007; Shen & Liu 2012; Trakhtenbrot & Netzer 2012). Since L_{5100} and L_{1350} are tightly correlated due to the homogeneity of the quasar continuum shape (Shen & Liu 2012), the lack of correlation between Hβ and CIV masses stems from the lack of a relationship between Hβ and CIV line widths[1]. In contrast, MgII line widths are much better correlated

[1]The comparison between single-epoch measurements of Hβ and CIV is somewhat controversial, as two studies have reported a strong relationship between Hβ and CIV line widths (Vestergaard & Peterson 2006; Assef et al. 2011). Shen & Liu (2012) consider these measurements in the context of other comparisons between Hβ and CIV. They find that when all measurements are considered together, Hβ and CIV line widths are not well-correlated (see their Figure 9). The quasars from Assef et al. (2011) and Vestergaard & Peterson (2006) make up just one quarter of the sample. Moreover, the Vestergaard & Peterson (2006) sample is highly biased towards fainter quasars with narrower Hβ and CIV lines. It is possible that a relationship between Hβ and CIV width exists at low luminosity and line width, but disappears at higher luminosities. In this thesis, I am concerned with the applicability of the mass estimates to large samples of high-redshift quasars, which will necessarily be strongly biased towards high luminosity quasars due to the observational limitations of survey data. As a result, the strong relationship reported in Vestergaard & Peterson (2006) is not relevant

with Hβ (Shen & Liu 2012; Trakhtenbrot & Netzer 2012; Shen 2013), indicating that MgII is a suitable line for estimating single-epoch virial masses.

One explanation for the lack of agreement between Hβ and CIV masses is the presence of a non-virialized, non-reverberating component in the CIV line (Denney 2012). Using a reverberation-mapped sample, Denney (2012) finds little agreement between the CIV FWHM determined from the rms spectrum and the CIV FWHM determined from the mean spectrum.[2] Since the rms spectrum measures the virialized component of the CIV line, this suggests that single-epoch measurements of the CIV line, which are most similar to the mean spectrum, are contaminated by the non-reverberating component and are therefore a poor measurement of the virial velocity. This result reconciles the conflicting results of Shen (2013) and Wilhite et al. (2007) and Peterson et al. (2004): Shen (2013) and Wilhite et al. (2007) test the virial assumption using FWHM from single-epoch spectra, while Peterson et al. (2004) measures FWHM using rms spectra. Therefore, while the rms spectra show evidence of virial motion in CIV, the single-epoch spectra do not, and correcting the single-epoch spectra appears to be more complicated than simply subtracting a narrow-line component.

This evidence has led to a growing consensus that single-epoch virial masses based on Hβ and MgII are reasonably free of systematic errors, but CIV masses are considerably less reliable. The discrepancies between CIV and Hβ line widths are believed to arise from physical differences between the Hβ and CIV emitting regions. CIV has a significantly higher ionization potential (64.49 eV) than either Hβ (13.60 eV) or MgII (15.04 eV). The BLR is believed to be stratified, with the high-ionization lines emitted closer to the central continuum source than the low-ionization lines, since the high-ionization lines have

---

to this work.

[2]The rms spectrum only measures the component of the line that varies over the reverberation timescale, since constant or very slowly varying components have an rms of zero and thus do not contribute to the rms spectrum. See Peterson et al. (2004) for a definition.

smaller reverberation lags than the low-ionization lines (Sulentic et al. 2000). Another difference between the high-ionization and low-ionization lines is the correlation between blueshift and ionization potential, with higher-ionization lines showing a larger blueshift than lower-ionization lines (Tytler & Fan 1992; Vanden Berk et al. 2001). The CIV blueshift is particularly well-studied and quite significant (Richards et al. 2011). The high-ionization line blueshift is thought to result from an outflow: the blueshifted line comes from the closer side of the outflow, while the redshifted far side of the outflow is obscured by the central continuum source (Sulentic et al. 2000). This is consistent with the finding of Denney (2012) that a significant portion of the CIV line does not reverberate, as the non-reverberating component is emission from the outflow.

The uncertainties in the single-epoch CIV virial masses are substantial. Direct comparisons between reverberation mapping masses and single-epoch CIV masses (e.g. Vestergaard & Peterson 2006) can only be made for the bright, nearby reverberation-mapped quasar sample. Since this sample is very different from our sample in both luminosity and redshift distribution, the error estimates of Vestergaard & Peterson (2006) are not relevant for this work. Instead, we must rely on comparisons between single-epoch CIV and Hβ masses. These comparisons yield CIV-Hβ scatter ranging from 0.3 decades (Netzer et al. 2007) to 0.5 decades (Trakhtenbrot & Netzer 2012; Denney et al. 2013). These comparisons are somewhat controversial, as Denney et al. (2013) find substantially better agreement between CIV and Hβ (0.2 decades) if the line dispersion is used rather than the FWHM, and if high signal-to-noise data is collected (S/N $\approx$ 50). These are valid considerations if high-S/N data and high-confidence measurements of the line dispersion are available (these generally go hand in hand, as line dispersion measurements are considerably more sensitive to spectral quality than FWHM measurements (Shen & Liu 2012)). However, in this work we consider the application to large surveys such as SDSS, where the typical signal-to-noise is much lower than required by Denney et al. (2013) (typical S/N is 10 for high redshift quasars in SDSS DR7 (Shen et al. 2011) and lower for BOSS). Therefore, the results of Denney et al. (2013) for the low signal-to-noise sample using mass estimates based on CIV

FWHM are more relevant to our work.

The dispersion between Hβ and CIV single-epoch masses is approximately the sum in quadrature of the uncorrelated uncertainties in the Hβ and CIV masses. The uncertainties in Hβ masses arising from fitting errors, intrinsic variability, and the Hβ radius-luminosity relationship are approximately 0.2 decades (Denney et al. 2009; Park et al. 2012). This means that the uncertainties in the CIV masses are ≈ 0.45 decades, arising from uncertainties in the CIV radius-luminosity relationship, virial assumption, fitting errors, and intrinsic variability. Presumably, the virial assumption is the dominant source of uncertainty, because of the presence of non-virial motions from outflows (Sulentic et al. 2000) and the poor relationship between changes in continuum luminosity and changes in line width (Shen 2013; Wilhite et al. 2007). In addition to this uncertainty, we must also add the calibration uncertainty in the virial coefficient f, which is essentially the error arising from the uncertainty in the reverberation mapping masses. This error is estimated to be 0.3-0.4 decades (Vestergaard & Peterson 2006; Woo et al. 2010; Park et al. 2012), leading to an absolute error of 0.55-0.6 decades in the CIV masses.

These concerns about the CIV line motivate us to use accretion disk models to find the black hole masses of our $z > 2.5$ quasar sample. For quasars at these redshifts, the UV peak at 1100 Å is redshifted into the optical, suggesting that accretion disk models may be especially effective for this high-redshift sample. While accretion disk masses are nowhere near as popular as virial masses, a number of authors have attempted to use accretion disk models to determine black hole masses. Malkan (1983) was the first to measure black hole masses using accretion disk models, using a Shakura & Sunyaev (1973) disk model with general relativistic corrections and fitting the black hole with both the Schwarzschild metric (zero spin) and Kerr metric (spin = 0.998). Malkan (1983) found a mass of 2-5 $\times$ 10^8 $M_\odot$ for 3C273, in good agreement with the current reverberation-mapping estimate of 7-8 $\times$ 10^8 $M_\odot$ (from the database of Bentz & Katz 2015). Sun & Malkan (1989) applied a similar method to optical, infrared, and ultraviolet spectroscopy from 60 quasars and Seyfert

galaxies. Their fits performed quite well: they estimated the mass and accretion rate to within 10% errors and reported that the quasar luminosity did not exceed the Eddington limit set by the fitted mass. Furthermore, they found that the mass was 2.5 times greater for the Kerr metric than for the Schwarzschild metric, and, correspondingly, the accretion rate was 2.5 times smaller for the Kerr metric. In contrast, Laor (1990), fitting similar accretion disk models to the spectroscopy of 101 quasars, found that the mass, accretion rate, and disk inclination are poorly constrained, with uncertainties of up to a factor of 10, as a result of more conservative assumptions about uncertainties. However, Laor (1990) did find that the accretion disk models were able to fit 80% of the quasars in his sample, constraining intrinsic dust emission to $E(B-V) < 0.15$. More recently, Ghisellini et al. (2010) measured the black hole masses of 10 blazars using photometry from *Swift*, constraining the masses to within a factor of two, not including systematic uncertainties such as the spin of the black hole, the possibility of a slim or thick disk radiating at a significant fraction of the Eddington luminosity, or the possibility that the spectrum at each annulus is a modified blackbody rather than a blackbody. Similarly, Castignani et al. (2013) measured the black hole masses of 79 $z < 2$ flat-spectrum radio quasars using photometry across a wide variety of wavelengths, including data from WMAP, Planck, WISE, SDSS, and GALEX, finding good agreement between the accretion disk masses and the single-epoch virial masses reported for the DR7 quasar catalog in Shen et al. (2011) (most of which were based on MgII and Hβ). Last, Calderone et al. (2013) measured black hole masses by fitting accretion disk models to the SDSS spectra of 23 narrow-line Seyfert type 1 galaxies at $0.1 < z < 0.8$; they also used photometry from WISE and GALEX to constrain emission from other components. They find uncertainties of 0.3–0.5 dex on average.

Motivated by this previous work, I attempt to accurately estimate black hole masses by fitting accretion disk models to our sample of quasars at $z > 2.5$. My methods differ from those of previous workers in several ways: I use medium-resoution spectroscopy rather than photometry; I use observations at only a single epoch (eliminating concerns about quasar variability); I fit near the peak of the accretion-disk spectrum, alleviating concerns

about the restricted range in wavelength over which I fit; and I study quasars for which the single-epoch virial masses are particularly suspect. I also use a relatively simple disk model, in order to reduce the complexity of the fit. Last, I present a more comprehensive understanding of the error budget for accretion disk masses than previous work.

2. Data

2.1. SDSS spectra

We estimate black hole masses using quasar spectra from the Sloan Digital Sky Survey (SDSS) (York et al. 2000). SDSS imaged 11663 deg^2, mostly at high Galactic latitudes near the North Galactic pole, in 5 bands (*ugriz*, Fukugita et al. 1996) using a 2.5-m telescope at Apache Point Observatory in New Mexico (Gunn et al. 2006). Quasar targets were selected from the imaging (Richards et al. 2002), confirmed spectroscopically (Stoughton et al. 2002), and identified as quasars if they have $M_i > 22.0$, and either one broad line with FWHM > 1000 km s^{-1} or interesting absorption features (Schneider et al. 2010). We use quasars from the DR7 catalog (Schneider et al. 2010; Shen et al. 2011). Quasar targets were selected in several different ways (see Table 27 in Stoughton et al. 2002; Richards et al. 2002):

1. Point sources matching a FIRST detection with $i < 19.1$.

2. Sources with significantly different colors than stars or galaxies; *ugri* colors are used for low-redshift sources and *griz* colors are used for high-redshift ($z \gtrsim 3$) sources. Additionally, sources must have $i < 19.1$ (low-redshift) or $i < 20.2$ (high-redshift candidates).

3. Serendipitous algorithms selecting outliers in color space not identified by the quasar color-selection algorithm, or serendipitous FIRST matches.

4. Matches to ROSAT sources.

Additionally, some sources targeted as stars or galaxies were found to be quasars and included in the quasar catalog.

The completeness of the survey varies depending on the selection criteria; most notably, the completeness of color-selected quasars drops significantly at $z \sim 2.7$ and slightly at $z \sim 3.5$, and blue quasars are preferentially selected at $2.2 < z < 3$ (Richards et al. 2006).

The radio-selected quasars exhibit no such drop in completeness because they are not targeted using object colors. Of the quasars in the radio-loud sample, 49 were selected either based on their colors or as FIRST matches, 21 were selected only based on FIRST matching, and the remaining 16 were selected via various other algorithms[3]. In contrast, the radio-quiet quasars were required to be either color-selected or serendipity-selected; 80 were color selected and 6 were serendipity selected. As a result, differences between the radio-loud and radio-quiet samples may be attributable to selection effects.

After the targets are selected, they are assigned to plates using the tiling algorithm (Blanton et al. 2003); not all detections with target flags are chosen as spectroscopic targets. Next, targets are observed on a twin multi-object fiber-fed spectrograph with wavelength range 3800 to 9200 Å (Smee et al. 2013), sky subtracted, corrected for telluric absorption, and spectrophotometrically calibrated (Stoughton et al. 2002). Spectra are binned equally in log-λ space with 69 km s^{-1} per pixel, wavelength calibration is accurate to 5 km s^{-1}, and spectral resolution ranges from 1850 to 2200 (Stoughton et al. 2002). Spectrophotometric calibration is accurate to 4% for point sources, although the calibration errors are greater for blue wavelengths than for red wavelengths (Adelman-McCarthy et al. 2008)[4]. Spectrophotometric calibration is also significantly impacted by Na D absorption from the interstellar medium at 5890 Å, and night sky emission lines at 5577 Å, 6300 Å, 6363 Å, and the OH forest at $>$ 6700 Å. To reduce the impact of these lines, we remove regions 6 Å on either side from the lines at 5577 Å, 5890 Å, 6300 Å, and 6363 Å (following Calderone et al. 2013). We also remove all pixels with nonzero single-pixel spectroscopic mask flags (see Table 11 of Stoughton et al. (2002) for a description of the flags). We use

[3]Of these, 9 were serendipitous FIRST matches, 2 were color outliers not flagged as quasar targets, 3 were both FIRST matches and color outliers, 1 was targeted as a galaxy, and 1 was a ROSAT match.

[4]See also `http://classic.sdss.org/dr7/products/spectra/spectrophotometry.html`

the dereddened spectra of Shen et al. (2011)[5], who correct for Galactic extinction using the Cardelli et al. (1989) extinction law with $R_V = 3.1$ and $E(B-V)$ from the Schlegel et al. (1998) dust map.

2.2. Radio loud and radio quiet samples

The radio loud quasar sample is drawn from the Gobeille et al. (2014) catalog, which consists of 123 radio loud quasars at $z > 2.5$. These quasars were selected from the NASA/IPAC Extragalctic Databse (NED) to lie roughly within the SDSS imaging region (7 to 17.5 hr in RA and 0 to 65 deg in DEC) and have 1.4 or 5 GHz flux density greater than 70 mJy. Of this sample, 86 are included in the SDSS DR7 quasar catalog, and the other 37 lack SDSS spectra. Our radio loud sample consists of the 86 SDSS-confirmed quasars from the Gobeille et al. (2014) catalog, lying at $2.5 < z < 5.28$ (see Table 3 for a list of sources). We also select 86 matched radio-quiet quasars at $2.5 < z < 5.28$ from the DR7 catalog, defined as quasars lying within the FIRST coverage region but lacking a FIRST detection (see Table 4 for a list of sources). These quasars have 1.4 GHz flux density below the FIRST detection limit of 1 mJy (Becker et al. 1995) and were matched to the radio-loud quasars in redshift and luminosity (see Figure 1). Radio loudness can be defined either using R, the ratio of rest-frame 6 cm flux to rest-frame 2500 Å flux ($R > 10$ for radio-loud quasars, e.g. Stocke et al. 1992), or using the rest-frame 6 cmluminosity density ($L_{rad} > 10^{25}$ W Hz^{-1}, e.g. Miller et al. 1990; Hooper et al. 1995). All quasars in the radio loud sample meet both radio loudness criteria (Figure 2) and are substantially brighter in the radio than the radio-quiet quasars.

[5]Spectra are publicly available here: `http://das.sdss.org/va/qso_properties_dr7/data/dered_spectra/`

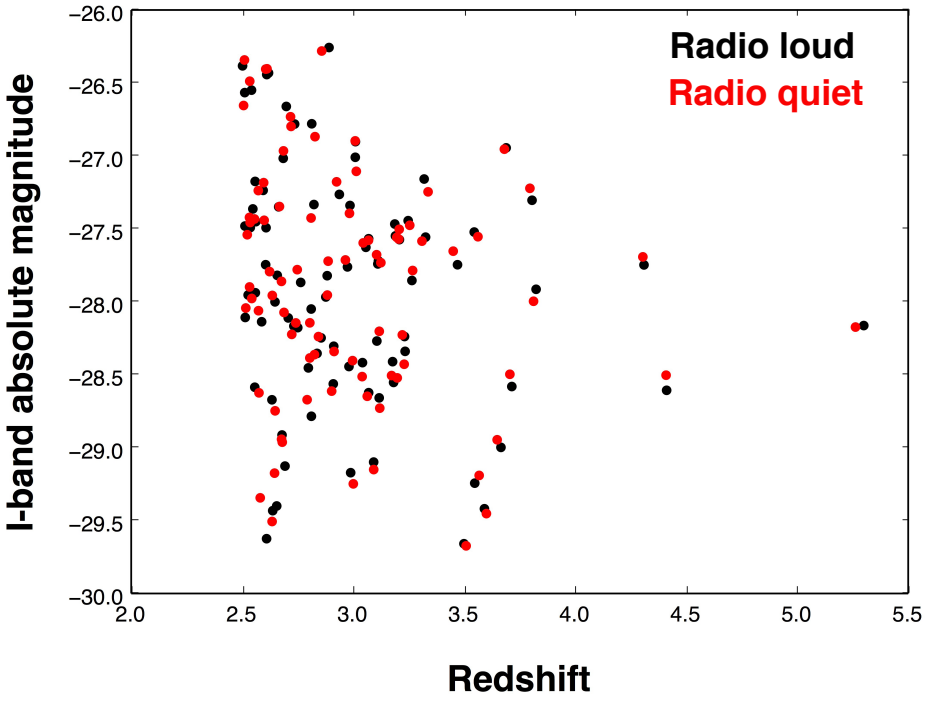

Fig. 1.— Redshift and luminosity distribution for radio-loud (black) and radio-quiet (red) samples. The selection process ensures that the redshift and luminosity distributions are essentially identical for the radio-loud and radio-quiet sources.

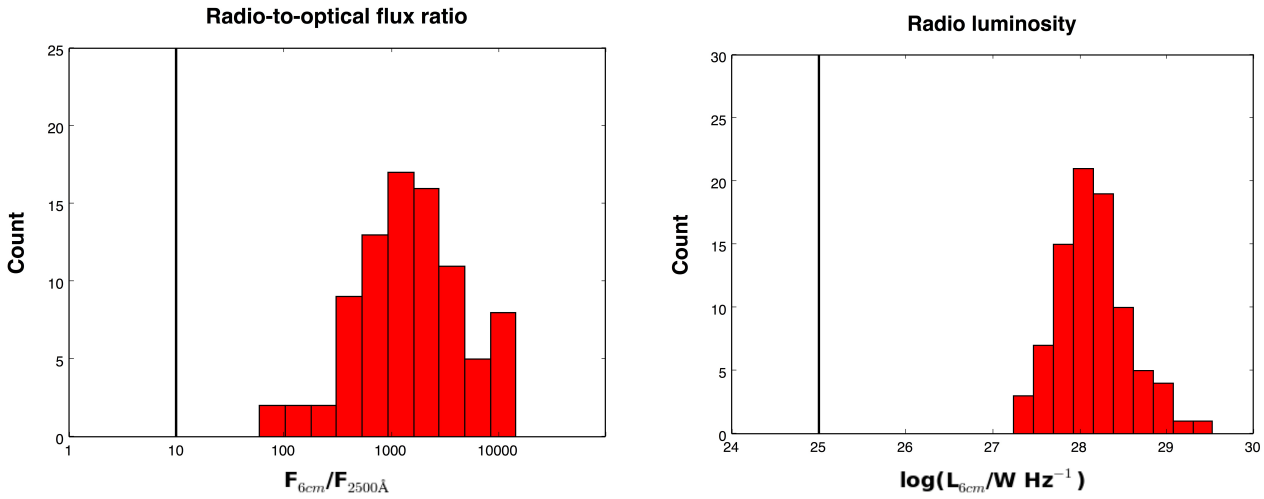

Fig. 2.— Radio-to-optical flux ratio R (left) and radio luminosity L_{rad} (right) for the radio-loud quasars. Vertical lines are standard thresholds for radio loudness, $R = 10$ and $L_{rad} = 10^{25}$ W Hz^{-1}. Flux densities were computed using the Gobeille et al. (2014) VLA measurements and converted to rest-frame 6 cm flux density assuming a power-law slope $\alpha = -0.5$.

3. Methods

3.1. Disk model

We fit a thin accretion disk model to each spectrum in order to determine the maximum disk temperature and the black hole mass. As gas falls into the black hole, its gravitational potential energy is first converted to kinetic energy and then radiated as heat due to dissipation from viscous torques. Since the accretion disk rotates differentially, each annulus exerts a torque on its neighbors, and the work done by the net torque on an annulus is radiated as heat. In the thin disk approximation, several assumptions are made to calculate the spectrum. The disk is assumed to be cylindrically symmetric with negligible vertical extent, and it is assumed to be in a steady state where the mass and angular momentum of each infinitesimally thin annulus are constant in time. Under these approximations, the dissipation from each side of the disk can be written (Frank et al. 1992):

$$D(R) = -\frac{\dot{M}\omega R}{4\pi}\frac{\mathrm{d}\omega}{\mathrm{d}R}\left(1 - \frac{\omega(R_{in})R_{in}^2}{\omega R^2}\right) \tag{3}$$

where R is the radius of the annulus, $\dot{M}$ is the accretion rate, and $\omega(R)$ is the angular velocity of the gas in each annulus, as computed from the central potential. If the energy dissipated is radiated as heat, we can compute the effective temperature at each radius:

$$D(R) = \sigma T(R)^4 \tag{4}$$

where σ is the Stefan-Boltzmann constant. If the disk is also optically thick in the z-direction, the vertical structure of the disk does not matter, and the spectrum can be computed by summing the spectra arising from each annulus. If each annulus radiates as a blackbody, the spectrum is given by the integral of a Planck function $B_\nu(T)$:

$$F \propto \int_{R_{in}}^{R_{out}} B_\nu(T(R))R\,\mathrm{d}R \tag{5}$$

where R_{in} is the inner radius and R_{out} is the outer radius. We assume a non-rotating (Schwarzschild) black hole, with the inner radius fixed at $6R_g$ (where $R_g \equiv GM/c^2$), the

innermost stable orbit for a Schwarzschild hole. The outer radius is fixed at $1000R_g$, and does not measurably affect the spectrum.

In the standard treatment (Frank et al. 1992), the angular velocity $\omega(r)$ is Keplerian. However, this assumes a Newtonian potential throughout the accretion disk, and this assumption breaks down near the innermost stable orbit, where general relativistic effects are signfiicant. A more accurate approximation to the true general relativistic solution is the pseudo-Newtonian potential (Paczyńsky & Wiita 1980):

$$\phi(R) = -\frac{GM}{R - 2R_g} \tag{6}$$

where $R_g = \frac{GM}{c^2}$. The pseudo-Newtonian potential accurately models general relativistic effects, as it correctly reproduces the location of both the marginal stable circular orbit

$(6R_g)$ and the marginal bound orbit $(4R_g)$[6] and yields very accurate estimates of accretion efficiencies (Paczyński & Wiita 1980). The DISKPN model also also allows the radiation to be generalized as a modified blackbody:

$$I(\nu, T) = \frac{1}{f_{col}^4} B(\nu, f_{col}T) \tag{11}$$

where f_{col} is the color-temperature correction. The relationship between dissipation and temperature is also modified:

$$D(R) = \sigma \left(\frac{T}{f_{col}} \right)^4 \tag{12}$$

Since the disk is unlikely to be optically thick nor to radiate as a perfect blackbody, the modified blackbody is a useful approximation (Koratkar & Blaes 1999; Davis et al. 2006). In particular, the modified blackbody offers a rough phenomenological method to account for

---

[6]The effective potential for a particle with angular momentum L is given by:

$$U(R) = \phi(R) + \frac{L^2}{2R^2} \tag{7}$$

The orbital velocity is given by

$$\frac{1}{2}V^2 = E - U(R) \tag{8}$$

If the orbit is circular, V is constant, meaning that $\dfrac{\partial U}{\partial R} = 0$. Differentiating, this means

$$\frac{\partial \phi}{\partial R} - \frac{L^2}{R^3} = 0 \tag{9}$$

Given $\phi(R)$ (Equation 6), we can solve for L and write U solely as a function of R:

$$U = -\frac{GM}{R - 2R_g} + \frac{GMR}{2(R - 2R_g)^2} \tag{10}$$

This potential is greater than zero at $R < 4R_g$, so the marginal bound orbital radius is $4R_g$, exactly in agreement with the general relativistic result. This potential also has a local minimum at $R = 6R_g$, corresponding to the general relativistic result for the innermost stable circular orbit. See also Abramowicz (2009) for a "derivation" starting from a general relativistic treatment.

inverse-Compton scattering, which increases photons' energies and thus shifts the spectrum towards higher energies. If $f_{col} > 1$, the modified blackbody spectrum is harder than a blackbody spectrum with the same temperature (see Figure 3). Previous results indicate that $f_{col} = 1.7$ for accretion disks around X-ray binaries (Shimura & Takahara 1995), and that f_{col} is somewhat lower for accretion disks around quasars (Done et al. 2012).

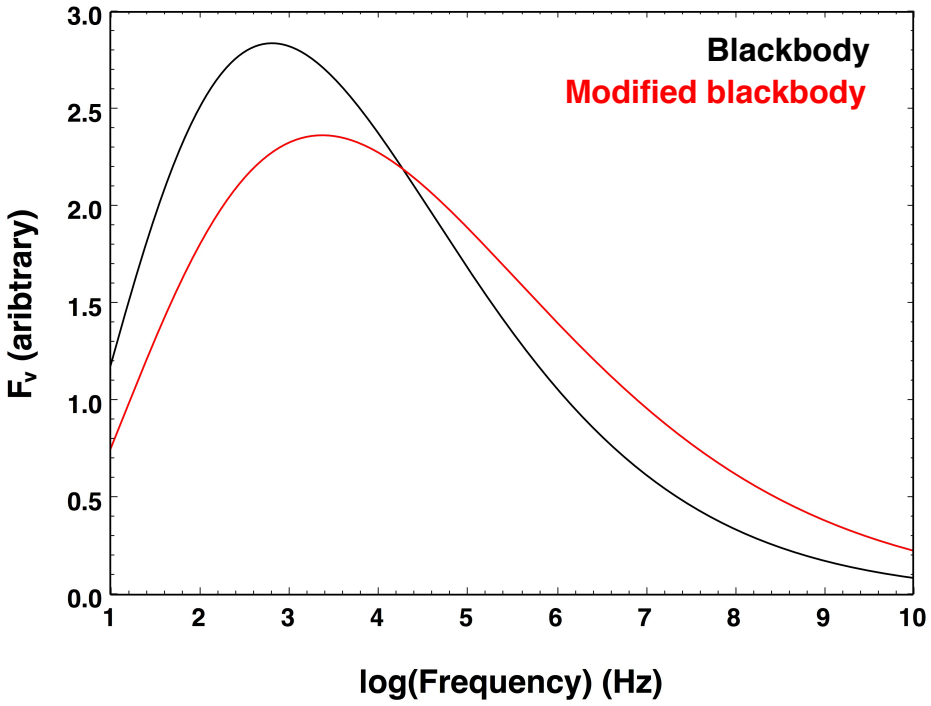

Fig. 3.— Blackbody (black) and modified blackbody (red) distributions. Note that the total flux is the same for both distributions: this is accomplished by the normalization of $1/f_{col}^4$ in Equation 11.

When fitting the DISKPN model to the spectra, the maximum disk temperature and normalization are free parameters. The black hole mass is related to the normalization:

$$K = \frac{4\pi}{h^3 c^2} \left(\frac{GM}{c^2 D} \right)^2 \frac{\cos i}{f_{col}^4} \tag{13}$$

where i is the inclination of the disk. The determination of i and f_{col}, and their associated uncertainties, will be discussed below in Section 5.

3.2. Spectral fitting procedure

We use SHERPA, a Python module for modeling and fitting, to fit our spectra (Freeman et al. 2001)[7]. Since SHERPA models are expressed in energy (keV) vs. photon flux (N_γ s^{-1} cm^2), we convert wavelength to energy and flux (reported in erg cm^{-2} s^{-1} $Å^{-1}$) to photon flux, and perform all fits in energy-photons space. Quasar emission in the rest-frame ultraviolet exhibits several features: continuum emission (which we attribute to the disk), broad emission lines (see Table 1); a "small blue bump" consisting of blended emission from hundreds of Fe II and Fe III transitions plus Balmer photorecombination emission (the "Balmer continuum"); narrow Lyα forest absorption lines blueward of 1216 Å; and in some cases, broad and narrow absorption lines redward of 1216 Å, some that are intrinsic to the quasars and others that result from absorption by metals in intervening systems. Some quasars (known as broad absorption line (BAL) quasars) exhibit very strong and variable broad absorption lines associated with the quasar itself, usually located at Mg II, C IV, or Si IV. Due to the strong absorption lines, it is difficult to determine the continuum emission in BAL quasars. None of the 86 radio-loud quasars are BALs, and we exclude BALs from selection in the matched radio-quiet sample.

In order to accurately fit the continuum, we first recover the absorption from the Lyα forest. The resolution of the SDSS spectra is insufficient to resolve the peaks and troughs of the Lyα forest; as a result, the observed transmission peaks in the SDSS spectra are partially blended with absorption troughs and are therefore not good measurements of the continuum flux. Fortunately, in order to accurately measure the Lyα forest, tools have been developed to determine the continuum flux. We use the the publicly-available mean-flux regulated PCA continuum fits of Lee et al. (2012)[8] to estimate the continuum from 1030-1216 Å for nearly all DR7 quasars with $z > 2.3$. These fits are generated in two

[7]See also `http://cxc.harvard.edu/sherpa4.4/`

[8]ftp.astro.princeton.edu/lee/continua/

steps. First, Lee et al. (2012) fit linear combinations of the PCA eigenspectra templates of Suzuki et al. (2005) and Pâris et al. (2011) to each quasar spectrum, using only the red side of Lyα (1216-1600 Å). Since the weak emission lines on the blue side of Lyα are correlated with the weak emission lines on the red side, the continuum shape is well modeled. Next, they adjusted the continuum to match measurements of the Lyα forest opacity as a function of redshift ("mean-flux regulation"). Since Lee et al. (2012) only gives the fitted continuum as a function of wavelength, we simulate noise in the spectrum by replacing each point in the range 1030-1216 Å with a random number drawn from a Gaussian distribution. The mean of the distribution is equal to the extinction-adjusted Lee et al. (2012) continuum flux at that wavelength and the standard deviation given by the SDSS pipeline measurement error at that wavelength.

Nine of the radio-loud quasars lack Lee et al. (2012) fits due to a flag indicating problems with the spectrum: eight have bad columns in more than 10% of the pixels, and one has low counts in the fiber flat. Of the remaining 77 spectra, nine were flagged by Lee et al. (2012) as problematic fits, so we do not correct these spectra for Lyα forest absorption and thus do not include them in our sample, leaving us with 68 radio loud quasars. Three of the radio-quiet quasars lack Lee et al. (2012) fits, with all three having bad columns in more than 10% of the pixels, while eight other radio-quiet quasars are flagged by Lee et al. (2012) as problematic fits, leaving us with 75 radio quiet quasars. Using mock spectra, Lee et al. (2012) estimates that the errors in the Lyα forest continuum are $\approx 5\%$, increasing with higher redshift and lower signal-to-noise. The assumed opacity of the Lyα forest as a function of redshift ($\tau(z)$) is an additional source of uncertainty, not included in the Lee et al. (2012) error estimates of $\approx 5\%$. In Section 5.5, we estimate the impact of this uncertainty on the mass estimates.

After reconstructing the continuum from the Lyα forest, we use a three step process to fit the disk models to the continuum, removing both the narrow absorption lines and the broad emission lines before fitting the disk model, iron template, Balmer continuum, and

Table 1.

Line ID	λ (Å)	Fitted with strong or weak lines
Ar I	1065	weak
Fe III	1117	weak
C III*	1175	strong
Lyα	1216	strong
N V	1240	strong
Si II	1265	strong
O I/Si II	1305	weak
C II	1335	weak
Si IV/O IV]	1399	weak
N IV]	1486	strong
C IV	1549	strong
He II	1640	strong
O III]/Al II/ Fe II	1663	strong
N III]	1748	weak
Al III	1857	strong
Si III]/Fe III	1892	strong
C III]	1906	strong

Note. — Line IDs and wavelengths from Vanden Berk et al. (2001) and Netzer (1990).

weak emission lines to the resulting spectrum. We manually remove narrow absorption lines by marking the center of each line and removing all points 0.02 eV from the line center on either side. We find that manual removal provides the most reliable and effective removal of the narrow absorption lines.

Next, we remove the regions around the strong emission lines C IV 1549 Å, C III] 1906 Å, Lyα 1216 Å, and N V 1240 Å. We fit Gaussians to the strong emission lines and their weaker (and often blended) neighbors, C III* 1175 Å, Si II 1265 Å, N IV] 1486 Å, He II 1640 Å, O III] 1663 Å, Al III 1857 Å, and Si III] 1892 Å. We fit a model consisting of Gaussians for each of the previously mentioned lines; additional Gaussians at 1216 Å and 1549 Å to properly fit asymmetries in Lyα and C IV; the XSDISKPN model for continuum emission from the disk; and the Vestergaard & Wilkes (2001) iron template. We place physical constraints on the emission lines. The FWHM must be between 1 and 50 Å, the position is allowed to vary by 30 Å in either direction for the strong lines and 15 Å for the weak lines, and the amplitude is forced to be positive. We use the Nelder-Mead direct search algorithm to find the minimum χ^2 for the model (Lagarias et al. 1998; Wright 1996)[9]. We find that this fitting method reproduces the shape of the Lyα, C IV, and C III] lines very well. We define the emission line region as the region over which the combined flux from the emission lines is greater than 10% of the average measurement error of the spectrum, and remove all points within this region for each emission line. We also remove the "1600 Å" bump between C IV and He II, since previous work has found that Gaussians from C IV and He II and the Vestergaard & Wilkes (2001) iron template cannot adequately model emission in this region (Fine et al. 2010).

In the third step, we fit to the remaining region, free of strong broad emission lines and

[9]See `http://cxc.harvard.edu/sherpa/ahelp/neldermead.html` for the SHERPA implementation of Nelder-Mead. To improve convergence, we use the strictest criteria for convergence, finalsimplex = 11. Additionally, we fit iteratively until $\Delta\chi^2 < 0.1$ between successive fits.

narrow absorption troughs. Our model consists of the XSDISKPN model; the Vestergaard & Wilkes (2001) iron template with the normalization as a free parameter; and Gaussians for the weak lines Ar I 1065 Å, Fe III 1117 Å, O I 1305 Å, C II 1335 Å, Si IV/O IV 1399 Å, and N III] 1748 Å. These lines are sufficiently weak to be fit adequately with only a single Gaussian. Note that we include Fe III 1117 Å separately from the iron template because the template does not include iron emission at wavelengths below 1250 Å. We place the same physical constraints on the Gaussians as before, except that we only allow the position to vary by 15 Å in either direction and the FWHMs of Ar I 1065 Å and Fe III 1117 Å are restricted to lie between 1 and 30 Å. While the Lee et al. (2012) continuum estimates extend to 1030 Å, we do not fit the spectrum below 1055 Å, allowing us to ignore the relatively strong Lyβ/O VI blend at 1033 Å. We found that fitting a Gaussian at the blue end of the spectrum sometimes led to spurious fits, since the Lee et al. (2012) continuum estimates only include about half of the Lyβ/O VI profile, causing the fits to be poorly constrained. Thus, we simply do not consider the Lyβ/O VI region between 1030 and 1055 Å.

Separately fitting the hundreds of UV iron transitions is impractical, so we instead use the empirical iron template of Vestergaard & Wilkes (2001), derived from HST spectroscopy of the nearby AGN I Zw 1. This is a standard method for estimating iron emission in quasar spectra. Since I Zw 1 is a narrow line object with a FWHM of 900 km s^{-1}, the iron model must be broadened before it is applied to each spectrum (Vestergaard & Wilkes 2001). We construct 15 broadened iron templates, with FWHMs ranging from 1000 to 15000 km s^{-1}, fit our model using each template with the overall normalization of the iron model as a free parameter, and choose the template that yields the lowest χ^2.

The iron emission and the Balmer continuum combine to form the "small blue bump" from 2000 to 4000 Å. The Balmer continuum arises from transitions between free electron states and bound states (hydrogen atoms) with $n = 2$. As a result, it is characterized by a gradual rise on the blue side of the 3646 Å Balmer edge (corresponding to the $n = \infty$ to $n = 2$ transition) and a steep drop on the red side. Previous work on modeling

the Balmer continuum has considered both optically thick and optically thin Balmer continuum emission (Grandi 1982) and has found that emission from the Balmer continuum is significant even at 2000 Å (Jin et al. 2012). We model the Balmer continuum using a partially optically thick model (as in Shen & Liu (2012)):

$$F(\nu) = AB_\nu(T_e)\left(1 - \exp\left(-\tau_{BE}\left(\frac{\nu_{BE}}{\nu}\right)^3\right)\right) \tag{14}$$

where B_ν is a Planck function with the electron temperature T_e frozen at 15000 K, ν_{BE} is the frequency corresponding to the 3646 Å Balmer edge, and the optical depth τ_{BE} and overall normalization A are free parameters. Following Shen & Liu (2012), τ_{BE} is constrained between 0 and 2. While we originally attempted to fit the spectra using a model consisting only of the accretion disk plus the Gaussians plus the iron model, this model was unable to accurately fit the spectra over the rest-frame wavelength range 900 to 2500 Å, necessitating the inclusion of the Balmer continuum component. We consider the effect of uncertainties in the shape of the Balmer continuum in Section 5.6.

Full convergence of the fit to the global minimum is necessary to accurately estimate confidence intervals for the fit parameters. To achieve optimal convergence, we use the Nelder-Mead algorithm using the strictest conditions for convergence and step sizes appropriate for each parameter. We begin by sequentially adding each component of the fit: first fitting the disk model, then the disk model plus the iron template, then the disk model, iron template, and Balmer continuum, then the disk model, iron template, Balmer continuum, and the first Gaussian, etc. Next we iteratively run the full fit until the difference in χ^2 between successive fits is less than 0.01. To reduce the runtime, we use the Levenberg-Marquardt algorithm for all iterations after the first. Nelder-Mead is significantly better at finding global minima than Levenberg-Marquardt, but also significantly slower. After the first iteration, the fit has converged to near the global minimum, so Levenberg-Marquardt is adequate for further approaching the minimum. Once we have found the global minimum, we estimate confidence intervals by fixing

the normalization and allowing the other parameters to vary freely[10], and finding the normalizations for which the χ^2 is equal to the minimum χ^2 plus one.

---

[10]In order to reduce the computation time, we fix the position and FWHM of all the Gaussians when estimating confidence intervals. Since the convergence method is not perfect at finding the global minimum, fixing the position of the Gaussians is necessary to ensure that all the fits find the same minimum. Additionally, freezing the positions and FWHMs of the Gaussians dramatically reduces computation time while only slightly harming the accuracy of the confidence interval estimation.

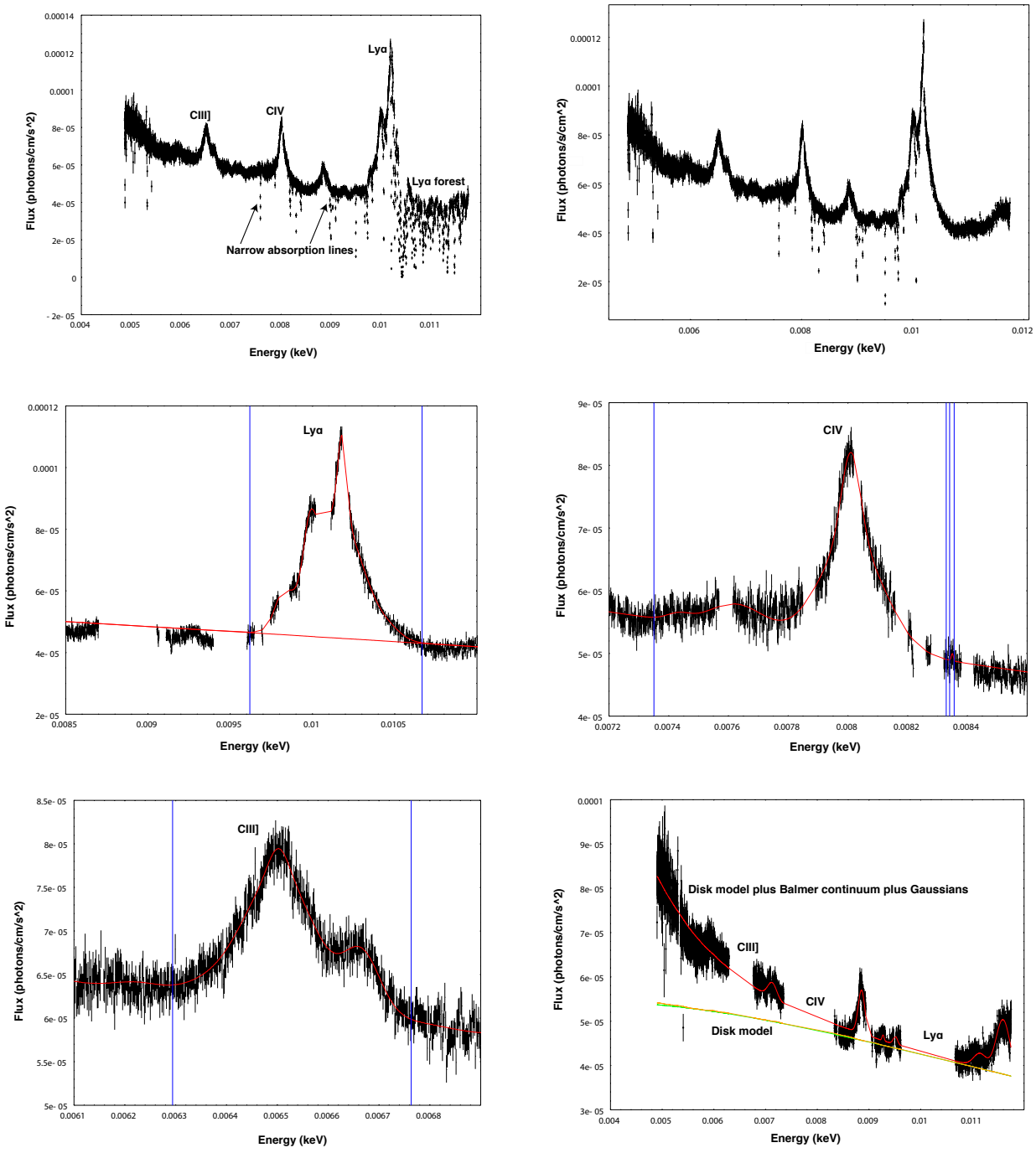

Fig. 4.— All panels depict the same object, SDSS082107.61+310751.1. *Top left*: Spectrum, with masked pixels and pixels near 5577 Å, 5890 Å, 6300 Å, and 6363 Å removed. The narrow absorption lines are marked and are later removed by hand. *Top right*: The Lyα forest correction. The continuum flux in the Lyα forest region is recreated using the Lee et al. (2012) continuum fits and accounting for noise by simulating each point as a Gaussian with the standard deviation equal to the reported error. We use this spectrum for all subsequent fits. *Middle left*: Lyα fit. The "Lyα region" that will be excluded from the final fit is indicated by the blue lines. *Middle right*: C IV fit. *Bottom left*: C III fit. *Bottom rightr*: Final fit. Note that the Lyα, C IV, and C III regions have all been removed. The accretion disk model is green, the accretion disk model plus the iron model is yellow, and the full model (accretion disk plus iron model plus Balmer continuum plus Gaussians) is red. This quasar displays an unusually strong Balmer continuum.

4. Fit results

We fit accretion disk models to the 68 radio-loud and 75 radio-quiet quasars with acceptable Lyα forest flux reconstructions from Lee et al. (2012). Nearly every fit was statistically acceptable; Figure 5 shows a histogram of the reduced χ^2 values for the entire sample. The median reduced χ^2 is 1.16. We investigate the four quasars with reduced $\chi^2 > 1.5$. Two of these quasars have high reduced χ^2 due to poor subtraction of the OH forest, creating unusually large outliers at the red end of the spectrum; the other two have poor fits of the iron model (the quasar with reduced $\chi^2 = 2.01$ has an unusually large FeIII UV48 bump at 2070 Å that is not modeled well by the Vestergaard & Wilkes (2001) template). However, all four quasars have reliable fits to the vast majority of the continuum, indicating that all quasars in the sample are adequately fit by our model.

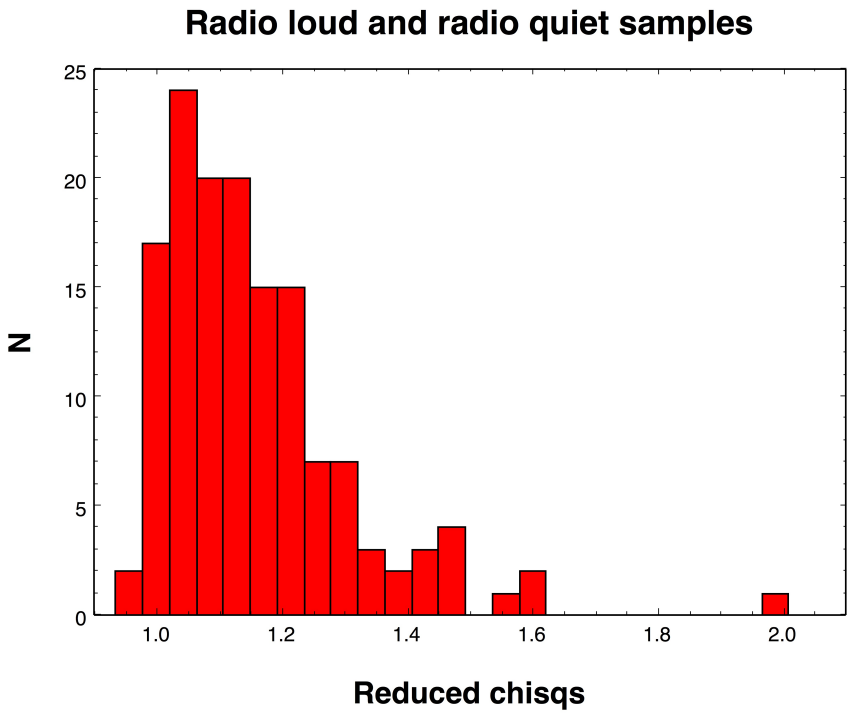

Fig. 5.— Reduced χ^2 for the 143 radio loud and radio quiet quasars fit with the DISKPN model.

Of the 143 quasars, two have non-physical fits, one radio-loud quasar, SDSS073320.48+272103.4, and one radio-quiet quasar, SDSS152004.05+151111.6. These quasars both have maximum temperatures in the keV range and masses in the range 10^3 to 10^5 $M_\odot$. These masses are grossly inconsistent with the quasars' observed luminosities, and produce X-ray fluxes that are far too great. We verify that the anomalous fits are not a result of poor convergence of the minimization algorithm by re-running both fits with an upper bound on T_{max} of 100 eV; in both cases, the best-fit has T_{max} equal to the upper bound, implying that the minimum χ^2 is indeed found at a very high T_{max}. As a result, we reject these anomalous fits as unphysical and do not consider these two quasars in further analysis. It is likely that the UV continuum in these two quasars does not come from thermal emission from a thin accretion disk, but rather from other sources, such as synchrotron emission for the radio-loud quasar or strong Comptonized emission from the soft X-ray excess for the radio-quiet quasar (e.g. Done et al. 2012).

We show two-dimensional χ^2 contour plots for the normalization and $T_{\rm max}$ as well as for the normalization and the Balmer continuum strength, for the same quasar as displayed earlier (Figure 6). While the normalization is quite degenerate with $T_{\rm max}$, it is not degenerate with the Balmer continuum strength (although as we will discuss in Section 5.6, the normalization is substantially affected by the shape of the Balmer continuum, set by the parameter T_e). The degeneracy between mass and maximum temperature is reflected in the distribution of mass and temperature results for the fits: quasars with large masses have small maximum temperatures, and vice versa (Figure 7).

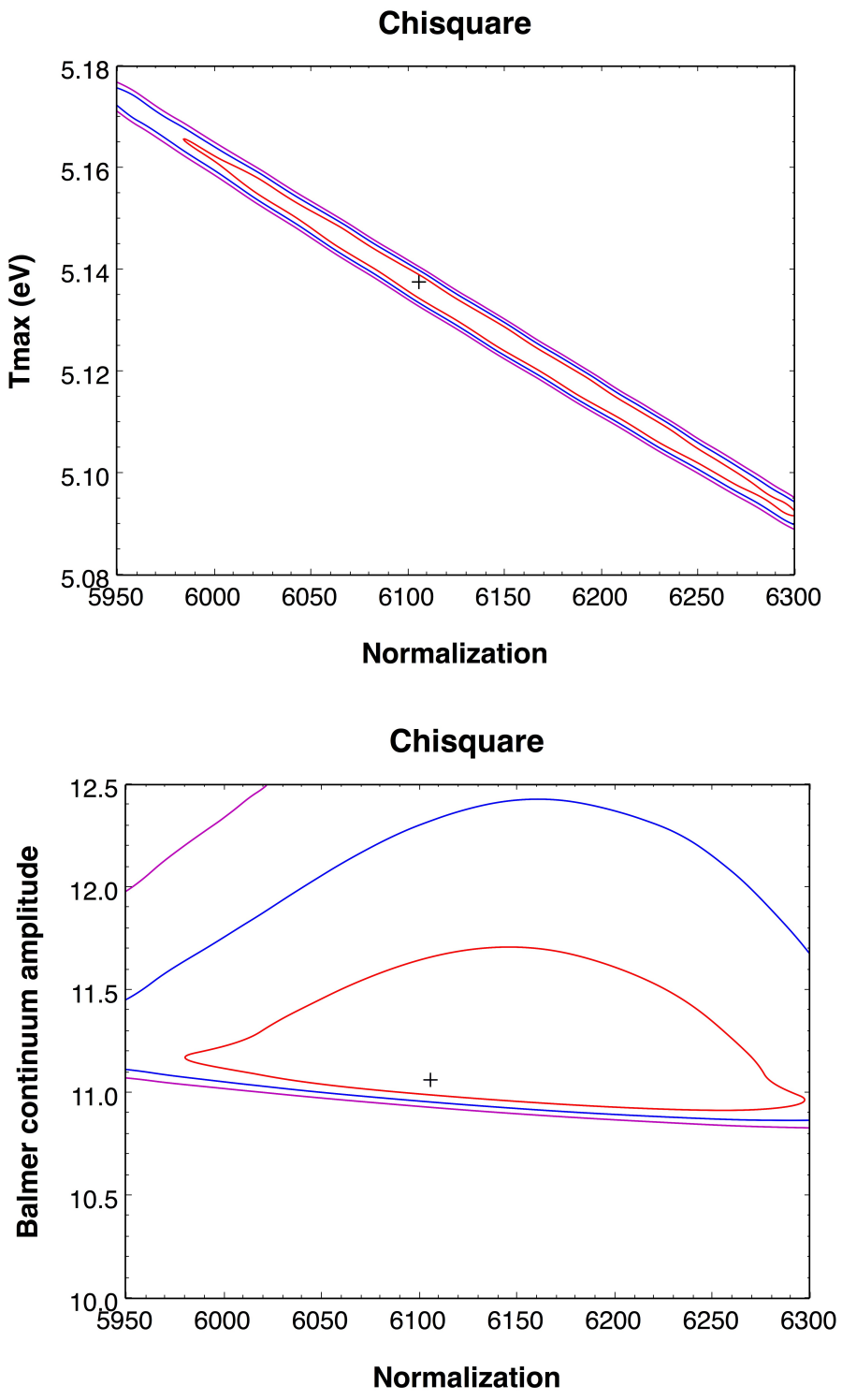

Fig. 6.— χ^2 contour plots for $T_{\rm max}$ and normalization, and Balmer continuum strength and normalization. Contour plots are for the fits to SDSS082107.61+310751.1. Contour are 1, 2, and 3 $\Delta\chi^2$ from the minimum (indicated by the black cross).

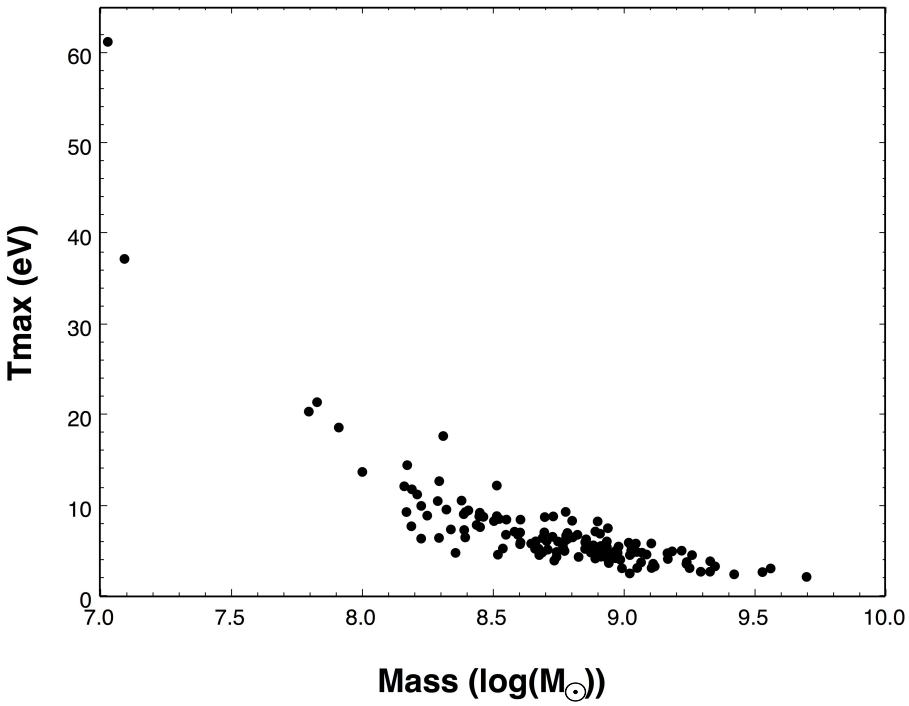

Fig. 7.— Distribution of $T_{\rm max}$ and mass for the 141 quasars with physical fits.

We compare the masses of the radio-loud quasars to the masses of the corresponding luminosity and redshift matched radio-quiet quasars. We use a total of 58 pairs for the comparison; of the remaining 28 pairs, one or both of the radio-loud and radio-quiet quasar lack a physical fit. The comparisons of the radio-loud and radio-quiet masses and their distributions are given in Figure 8. We find that the radio-loud and the radio-quiet quasars have identical masses to within measurement errors: the mean mass of the radio-loud quasars is 9.24 $\log M_\odot$ with a standard error of 0.05, while the mean mass of the radio-quiet quasars is 9.04 $\log M_\odot$ with a standard error of 0.05. The scatter between the radio-loud and radio-quiet masses is 0.45 decades. These results indicate that radio-loud quasars are substantially more massive than radio-quiet quasars with identical luminosities and redshifts. In contrast, the CIV virial masses for the radio-loud and radio-quiet samples are nearly identical: the mean virial mass for the radio-loud sample is 9.02 ± 0.17 $\log M_\odot$, while the mean virial mass for the radio-quiet sample is 9.24 ± 0.17 $\log M_\odot$.

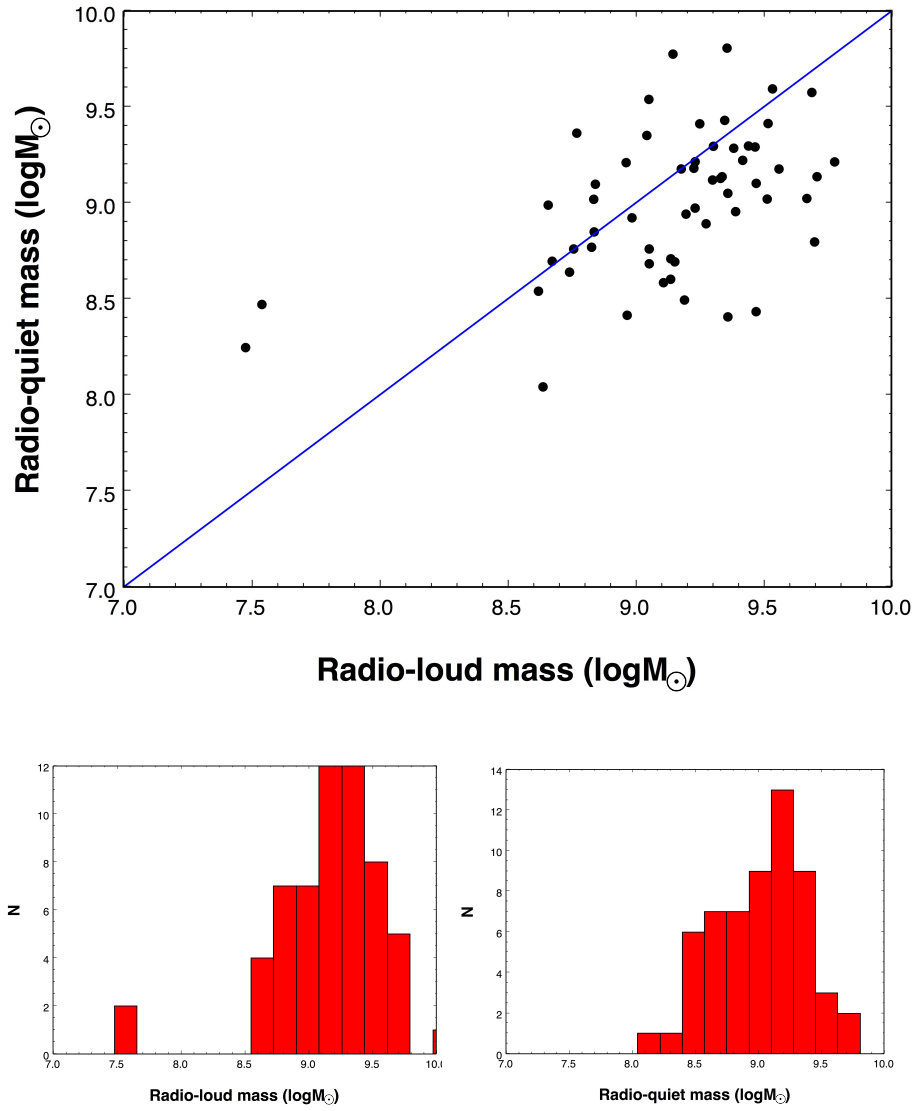

Fig. 8.— Comparison between the radio-loud and the radio-quiet samples for 58 pairs matched in redshift and luminosity with fits for both the radio-loud and radio-quiet quasar.

5. Sources of systematic error

In this section I will discuss several sources of systematic error in the disk mass estimates. These include contamination from the host galaxy; inclination effects; the color-temperature correction; black hole spin; the Lyα forest correction; the Balmer continuum; and intrinsic reddening. They are arranged in rough order of increasing severity.

5.1. Host galaxy emission

Emission from the host galaxy can contribute to the observed quasar SED, and must be removed to ensure accurate fitting of the accretion disk model. Host galaxy emission is most significant at low redshifts and luminosities, where the optical quasar luminosity may be comparable to or only slightly greater than the luminosity of a typical host galaxy. However, even at higher redshifts, the host galaxy contribution may still be significant for broad-line AGNs (Schneider et al. 2013).

We use the results of Schneider et al. (2013) to determine the host galaxy contribution for quasars in our sample. Using a sample of spectroscopically confirmed $0 < z < 4$ AGN from the COSMOS field (including both Type I and Type II AGN), Schneider et al. (2013) fit models to photometry ranging from the rest-frame IR (Spitzer) to the rest-frame UV (GALEX). These models consisted of the DISKPN model, host galaxy emission, and an empirical power law to account for IR emission from hot dust. For the host galaxy emission, Schneider et al. (2013) tried several different templates from the SWIRE library (Polletta et al. 2007)[11] and ultimately chose to fit every source using the Sb template, which provided the best fit on average. To ensure physically reasonable fits, Schneider et al. (2013) required the K-band flux to be less than 5 $M_\star$ at each redshift, ensuring that their derived host galaxy luminosities are consistent with past observations (Ridgway et al. 2001; Kotilainen

[11] `http://www.iasf-milano.inaf.it/~polletta/templates/swire_templates.html`

et al. 2009; McLeod & Bechtold 2009). For $2 < z < 4$ AGN, they find normalizations between 0.1 and 3, with template flux at 5500 Å normalized to 10^{-18} erg cm^{-2} s^{-1} Å^{-1} (see their Figure 14).

In order to estimate the host galaxy contribution, we compare the flux from the Polletta et al. (2007) Sb template, scaled by factors of 0.1, 1, and 3, to the observed flux from each quasar. As discussed above, these scaling factors are consistent with host galaxy K-band luminosities less than 5 $M_\star$, a range of luminosities supported by observations. We find that even at the highest normalization, the flux from the Sb template is at least two orders of magnitude lower than the flux emitted by any of the quasars in either the radio loud or the radio quiet sample (see Figure 9 for some examples). In contrast, Schneider et al. (2013) find significant host galaxy contribution in $\approx 10\%$ of their $z > 2.5$ quasar sample. However, the low host galaxy contribution that we find is entirely consistent with the results of Schneider et al. (2013), since they measure the host galaxy contribution in the rest-frame K band whereas we are concerned with the host galaxy contribution at 1000–2500 Å. The Polletta et al. (2007) Sb template peaks around 1 μm and declines sharply into the rest-frame UV, so the 2-10% contribution in the K-band found by Schneider et al. (2013) should correspond to a negligible contribution in the rest-frame UV.

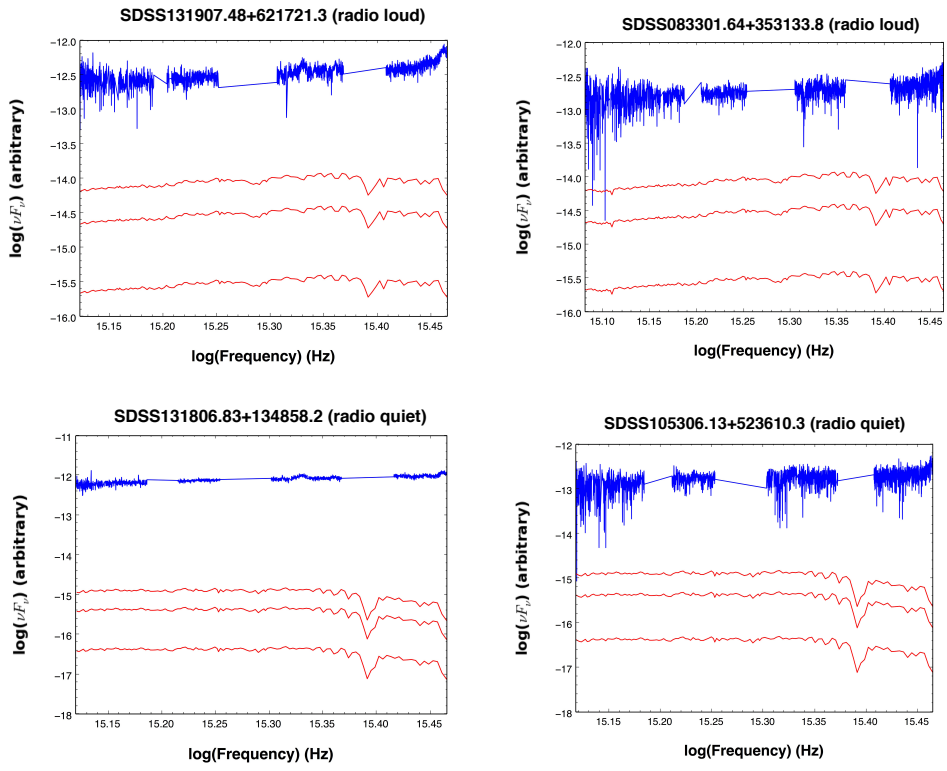

Fig. 9.— Comparison of quasar flux and host galaxy flux for four randomly selected quasars. The three red curves are the Sb template from Polletta et al. (2007), normalized at 5500 Å to 10^{-18} erg cm^{-2} s^{-1} Å^{-1} and scaled by 0.1, 1 and 3. The scaling factors are approximately the highest and lowest host galaxy scaling factors found by Schneider et al. (2013) in modeling the infrared to ultraviolet continuum emission from $2 < z < 4$ quasars.

The ratio of UV to K-band flux is very dependent on the assumed spectral type of the host galaxy, with later-type galaxies having more emission in the rest-frame UV than early-type galaxies. Low-redshift AGN exhibit a range of morphologies from early to late types (Gabor et al. 2009), so assuming that the Sb template adequately describes all quasar host galaxies is probably an over-simplification. We consider the differences between the Polletta et al. (2007) inactive galaxy templates, which include 7 spiral templates (S0, Sa, Sb, Sc, Sd, Sdm, and Spi4), 3 elliptical templates, and 3 starburst galaxy templates (modelled on M82, Arp 220, and NGC 6090). We normalize the flux of each template to the Sb template flux at 1 μm, since this is the wavelength at which the host galaxy

contributes the most to the observed quasar emission, and is therefore approximately the wavelength at which the Schneider et al. (2013) host galaxy normalizations are determined. We find that the UV flux for later-type galaxies, such as Sc, Sd, Sdm, and Spiral 4, is greater than the UV flux of the Sb template by up to a factor of 10. Therefore, we repeat our comparison between the observed quasar flux and the host galaxy flux using the Sdm template, which has the greatest UV flux, again using normalizations of 0.1, 1, and 3 (since the K-band flux is quite similar between the Sb and Sdm templates, these normalizations are still appropriate). We find that under the most generous assumptions (normalization of 3 and Sdm host galaxy), the maximum host galaxy flux is 10% of the quasar flux, while the median contribution is 2%. We emphasize that because AGN host galaxies span a wide range in morphology, these assumptions are likely met for at most only a few quasars in our sample; therefore, the host galaxy contribution is negligible for the vast majority of quasars in our sample. Furthermore, even for those few quasars with host galaxy contamination of a few percent, the error introduced by host galaxy contamination is dwarfed by the other systematic errors discussed below.

5.2. Nonrelativistic effect of inclination

The relationship between the mass and the normalization also depends on the inclination of the disk. In the nonrelativistic model such as DISKPN, changing the inclination merely changes the normalization of the spectrum by a factor of $1/\cos i$. However, relativistic effects will also change the shape of the spectrum as the inclination changes. In this section, we will only consider the non-relativistic change in intensity; see Section 5.4 below for a more complete treatment of the effect of inclination.

In the unified AGN model, broad-line and narrow-line quasars are identical except for their inclinations: the broad emission line region is obscured by a dusty torus in narrow-line AGNs, whereas broad-line AGNs are observed more nearly perpendicularly and thus are unaffected by obscuration from the torus. Since our sample is composed exclusively of

broad-line quasars, we expect that the disk will be oriented more nearly face on. The black hole mass is related to the orientation angle by a factor of $1/\sqrt{\cos i}$. If i ranges from $-60°$ to $60°$ (e.g. Davis et al. 2006) and $\cos i$ is uniformly distributed (as for isotropic orientation), this factor is on average 1.17, with standard deviation 0.12. However, quasars viewed more nearly face on will be brighter by a factor of $\cos i$, so a more appropriate distribution of $\cos i$ is a trapezoid with a peak at $\cos i = 1$ twice the value of the probability distribution function at $\cos i = 0.5$. The trapezoidal distribution results in a factor of 1.15 with a standard deviation of 0.11, which we will use in subsequent sections.

5.3. Color temperature correction

Inverse Compton scattering can lead to a substantial deviation from a blackbody spectrum, as electrons scatter photons to higher energies, converting the spectrum into a modified blackbody:

$$I(\nu, T) = \sqrt{\frac{\kappa_{\rm abs}(\nu, T)}{\kappa_{\rm es} + \kappa_{\rm abs}(\nu, T)}} B(\nu, T) \tag{15}$$

where $\kappa_{\rm abs}$ is the absorption opacity, $\kappa_{\rm es}$ is the Compton scattering opacity, and $B(\nu, T)$ is the Planck function. The absorption opacity decreases at higher frequencies, leading to a harder spectral shape. Creating an accretion disk model assuming that the radiation at each annulus follows Equation 15 rather than a Planck function requires knowledge of the vertical density profile of the disk, making the model considerably more complicated. A simplifying assumption is to replace Equation 15 with a color-temperature corrected blackbody, $I(\nu, T) = 1/f_{\rm col}^4 B(\nu, f_{\rm col} T)$, where $f_{\rm col}$ is the color temperature correction. Thus, the complicated problem of modeling the full vertical structure of the disk has been replaced by the simpler problem of finding the color temperature correction as a function of temperature.

At $T > 10^5$ K (≈ 8.6 eV), electron scattering opacity dominates absorption opacity, as thermal ionization of hydrogen provides a plentiful source of free electrons. For accretion

disks around black hole binaries, Davis et al. (2006) derive

$$f_{col} = \left(\frac{72}{T_{\rm keV}}\right)^{1/9} \tag{16}$$

While disks around black hole binaries are much hotter, with $T \approx 10^7$ K, Done et al. (2012) argue that Equation 16 applies to AGN accretion disks as well, although only at annuli in which electron scattering opacity dominates absorption opacity. However, Done et al. (2012) find that for annuli with lower temperatures, $T \approx 3 \times 10^4$ K (≈ 2.6 eV), the absorption opacity is very large because nearly all hydrogen is neutral at this temperature; thus, for $T < 3 \times 10^4$ K, the color temperature correction is essentially 1. Done et al. (2012) approximate $f_{\rm col}(T)$ using an empirical piecewise formula:

$$f_{\rm col}(T) = \begin{cases} \left(\frac{72}{T_{\rm keV}}\right)^{1/9} & T > 10^5 \text{ K} \\ \left(\frac{T}{3\times10^4}\right)^{0.82} & 3 \times 10^4 < T < 10^5 \text{ K} \\ 1 & T < 3 \times 10^4 \end{cases} \tag{17}$$

The result of Done et al. (2012) that $f_{\rm col}$ changes fairly rapidly with temperature at the temperature of an accretion disk about an AGN conflicts with the assumption of the DISKPN model that $f_{\rm col}$ is a constant. This is essentially true for accretion disks around black hole binaries due to the 1/9 exponent in Equation 16, but is a considerably worse approximation at the lower temperatures of the AGN accretion disk. Thus, the shape of the accretion disk spectrum will be distorted from the shape of the DISKPN spectrum. The Done et al. (2012) relationship for f_{col} also means that the average f_{col} will deviate from 1 for an AGN accretion disk. Since $M \propto f_{\rm col}^2$, this deviation could have a significant effect on the derived masses. While it is difficult to determine the detailed impact of Equation 17 on our masses without using a more sophisticated model, we can estimate its gross impact by using the temperature profile of each quasar to derive an average value of f_{col} appropriate for that quasar.

We can compute an average color temperature correction as a function of frequency:

$$\langle f_{\rm col} \rangle = \frac{\int_{R_{in}}^{\infty} f_{\rm col}(T(R)) T(R)^4 R \, {\rm d}R}{\int_{R_{in}}^{\infty} T(R)^4 R \, {\rm d}R} \tag{18}$$

where the averaging is performed over the disk luminosity at each radius, $\sigma T(R)^4$ (the Stefan-Boltzmann constant cancels in the numerator and denominator). Since the temperature fitting error is tiny compared to the black hole mass fitting error, the errors introduced in $f_{\rm col}$ from fitting uncertainties in the temperature will only be a few percent, far smaller than the other sources of error considered in this section. Most of the uncertainty arises from the modelling of $f_{\rm col}(T)$, and determining this uncertainty will require comparison with the fitting results from the Done et al. (2012) model. We will use the values of $f_{\rm col}$ obtained from Equation 18 to compute Eddington ratios and compare our masses to the virial masses of Shen et al. (2011) in Section 6.

5.4. Black hole spin and relativistic effects

The DISKPN model does not consider relativistic effects, and assumes that the black hole is non-rotating. Black hole rotation is characterized by the spin parameter a_*, which is the ratio between the angular momentum and the black hole mass; a_* ranges from -1 to 1. Recent results indicate that a_* is substantially different from zero for many supermassive black holes. Capellupo et al. (2015) fit thin accretion disk models to a sample of 30 quasars at $z \approx 1.5$, with the mass fixed from virial estimates and the accretion rate and spin as free parameters. While the uncertainty on the spin estimates is often quite large, they find quasars with well-constrained spins ranging from -1 to 1. Moreover, they find that for high-mass quasars ($M > 10^9 M_\odot$), a_* is well-constrained to be close to 1. This is consistent with the result of Trakhtenbrot (2014), who find that quasars with $M > 10^9 M_\odot$ have spins quite close to 1.

We study the effect of black hole spin on our fits using the KERRBB model of Li

et al. (2005). The KERRBB model differs from the DISKPN model in several ways: a_* is allowed to be nonzero; general relativistic effects such as frame-dragging, Doppler boosting, gravitational redshift, and bending of light close to the black hole are taken into account; and limb-darkening and self-irradiation are also taken into account. For comparison with the DISKPN results, we turn off the effects of limb-darkening and self-irradiation, set the inclination to 0° and the color-temperature correction f_{col} to 1. The zero-spin KERRBB fits are in excellent agreement with the DISKPN fits, with an r^2 of 0.971. The KERRBB masses are offset from the DISKPN masses by a small but significant amount: the DISKPN masses are 0.14 decades greater than the KERRBB masses. Once this offset is taken into account, the scatter between the DISKPN model and the KERRBB model is 0.16 decades. Overall, these results indicate that, at zero spin and face-on orientation, general relativistic effects have little impact on the ordering of masses in our sample, affecting only the absolute scale of the masses.

We run the KERRBB fits with five different values of a_*: -0.998, -0.5, 0, 0.5, and 0.998, and measure the difference in mass between the $a_* = 0$ fit and each of the other four fits. We find a median bias of -0.15 decades for $a_* = -0.998$ (i.e. if a_* is fixed at -0.998 the mass is 0.15 decades lower than for the zero spin case), -0.08 decades for $a_* = -0.5$, 0.12 decades for $a_* = 0.5$, and 0.41 decades for $a_* = 0.41$. The full distribution of deviations is given for each case in Figure 10. If the mass-spin relationships presented in Capellupo et al. (2015) and Trakhtenbrot (2014) are accurate and applicable to our sample, this analysis suggests that for lower-mass black holes ($M < 10^9 M_\odot$, essentially the lower-mass half of our sample), the uncertainty introduced by black hole spin is modest (0.1–0.2 decades) and the bias is zero, but that the masses reported for the higher-mass half of our sample are underestimated by 0.4 decades. Overall, this suggests that the uncertainty due to the a_* distribution is $\approx$ 0.2–0.3 decades. Note that the effect of the spin correction is very similar for all quasars in our sample, with standard deviations of $\approx$ 0.05 decades for the four distributions of mass difference.

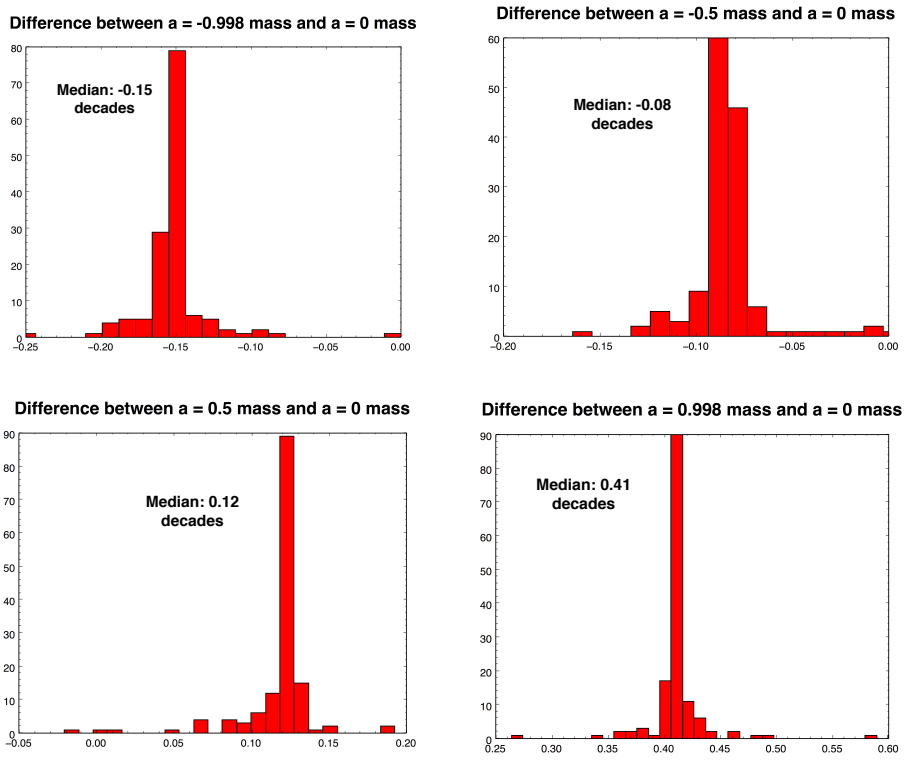

Fig. 10.— Distributions of the mass difference between spinning and non-spinning black holes for different values of spin parameter a_*. To better display the histograms, we do not show several outliers in mass difference: a -1.11 mass difference for $a_* = -0.998$; two -0.3 mass differences for $a_* = -0.5$; a -0.27 mass difference for $a_* = 0.5$; and a 0 mass difference for $a_* = 0.998$.

Inclination affects the mass slightly different in a general relativistic treatment than in a nonrelativistic treatment. The strong gravity of the central black hole bends light from the inner accretion disk. If the disk is viewed face-on, the observed flux from the inner accretion disk is therefore reduced. As the inclination angle changes, the flux from the inner accretion disk is increasingly bent into the line of sight, shifting the spectrum towards higher energies. We test the effect of inclination by running the KERRBB model for $i =$ 15, 30, and 45°. We differences of 0.01, 0.06, and 0.13 decades, similar to the nonrelativistic corrections of 0.02, 0.07, and 0.19 decades (obtained from $1/\sqrt{cosi}$. Since there is some dispersion about each inclination correction, the true uncertainty from inclination is likely

close to the nonrelativistic estimate of 0.11 decades.

5.5. Lyα forest correction

We use the Lee et al. (2012) estimates of the continuum blue of Lyα in order to correct for absorption from the Lyα forest. These estimates are based on fits to the continuum on the red side of Lyα, and therefore possess fitting uncertainties. In addition, since the estimates are adjusted to match the overall transmission of the Lyα forest, they are also affected by uncertainties in the Lyα forest transmission. We estimate the fitting errors using the results of Lee et al. (2012): in their Figure 8, they give the fractional uncertainty on the fits as a function of redshift and 1225–1600 Å signal-to-noise. We interpolate between the values on this plot to determine the fractional uncertainties in the fits. To determine the uncertainties on the Lyα forest transmission, we use the errors given in Faucher-Giguère et al. (2008) for $\tau(z)$ and propagate them to $F(z) \equiv \exp(-\tau(z))$. We then add the two sources of error in quadrature. We assume that the fitting and transmission errors are perfectly correlated from one pixel to another; while this is probably not strictly true, it is the most conservative assumption we can make, as a high covariance between neighboring pixels will lead to larger errors in our measurements than no covariance. To measure the effect of uncertainties in the Lyα forest correction, we adjust each pixel in the Lyα forest region by -2, -1, +1 and +2 σ. We plot the resulting distribution of mass differences in Figure 11.

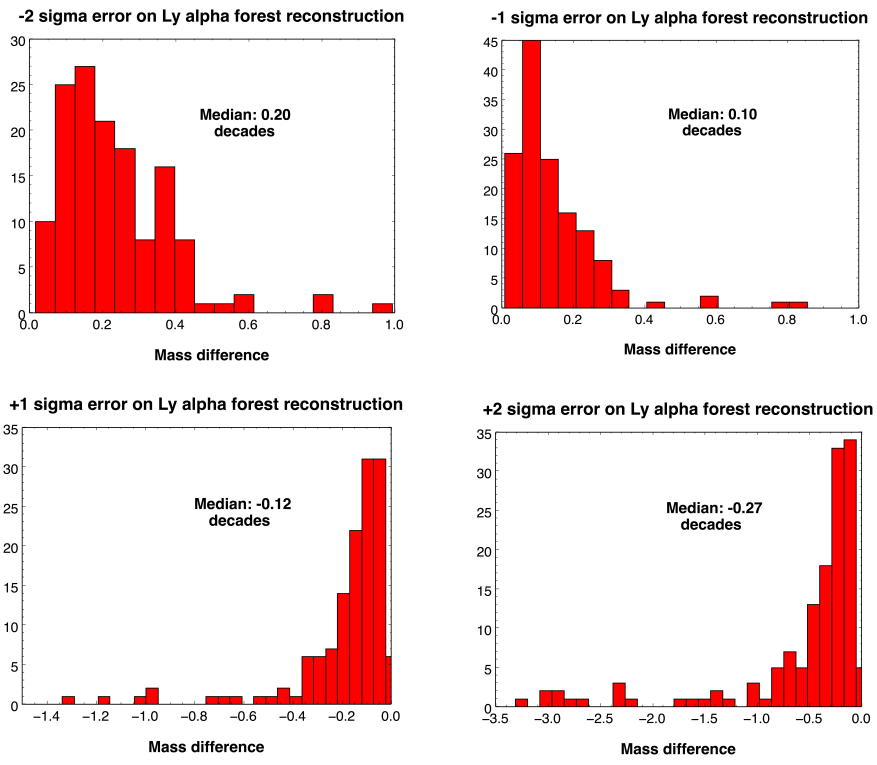

Fig. 11.— Distributions of the mass difference when the Lyα forest region is adjusted by -2, -1, +1, and +2 σ. To better display the histograms, we do not show several outliers in mass difference: three outliers at 1.14, 2.48, and 2.73 mass difference for -2 σ; two outliers at 1.85 and 2.5 mass difference for -1 σ; three outliers at -2.36, -1.69, and 2.51 mass difference for +1 σ; and one outlier at 2.5 mass difference for +2 σ.

Since the fitting errors on the Lee et al. (2012) Lyα forest correction are a function of redshift, we expect the uncertainty due to Lyα forest correction to vary as a function of redshift. We divide the sample into three equal length redshift bins and measure the median mass difference in each redshift bin, for -2, -1, +1, and +2 σ errors in the Lee et al. (2012) fits (Table 2). We find that the mass differences are quite similar for the low and medium redshift bins, but that the mass error is significantly higher for the high ($z > 3.07$)) redshift bin. Overall, the approximate 1 σ uncertainty from the Lee et al. (2012) Lyα forest correction is 0.1–0.15 decades in mass, or closer to 0.2 decades in mass for $z > 3$ quasars.

5.6. Balmer continuum

The Balmer continuum is a necessary but poorly constrained component of our model. Without the Balmer continuum, we would be unable to properly model the "small blue bump" at the longest wavelengths under consideration (≈ 2000-2500 Å). However, few previous studies have constrained the parameters of the Balmer continuum, and moreover, since we only fit at most half of its range, it is difficult for us to properly constrain its amplitude.

For all quasars with detectable Balmer continuum emission, we measured the ratio between the Lyα intensity (defined as the integral over the Lyα flux) and the Balmer continuum intensity, $I(\mathrm{Ly}\alpha)/I(\mathrm{BaC})$. For the 101 radio-loud and radio-quiet quasars with detectable Balmer continuum, we find a median Lyα to Balmer continuum ratio of 0.3, with a standard deviation of 0.35 (see Figure 12 for the distribution). This ratio has been previously studied both observationally and theoretically, though it is not particularly well-constrained by either observations or theory. Different models predict a wide range of possible ratios: Wills et al. (1985) predict $I(\mathrm{Ly}\alpha)/I(\mathrm{BaC}) \approx 10$, while Kwan & Krolik (1981) predict $I(\mathrm{Ly}\alpha)/I(\mathrm{BaC}) \approx 2$. Observed $I(\mathrm{Ly}\alpha)/I(\mathrm{BaC})$ values span nearly as wide a range, and suffer from sensitivity to the power-law continuum fit used and the wavelength range of observations. Wills et al. (1985) observe $I(\mathrm{Ly}\alpha)/I(\mathrm{BaC}) \approx$ 1-10, while Kwan & Krolik (1981) observe $I(\mathrm{Ly}\alpha)/I(\mathrm{BaC}) \approx$ 0.5-4. The largest sample and highest-quality

Table 2.

σ	Low z	Medium z	High z
-2	0.20	0.18	0.26
-1	0.10	0.10	0.13
+1	-0.09	-0.10	-0.19
+2	-0.19	-0.22	-0.48

Note. — Mass difference for different errors on Lyα continuum fit as function of redshift.

observations come from Tsuzuki et al. (2006), who find $I(\mathrm{Ly}\alpha)/I(\mathrm{BaC})$ ranging from 0.2 to 10 for a sample of 12 quasars, with a median $I(\mathrm{Ly}\alpha)/I(\mathrm{BaC})$ of 0.5. While our results for $I(\mathrm{Ly}\alpha)/I(\mathrm{BaC})$ are slightly lower than previous findings, they are well within the substantial error bars of previous results. Furthermore, it is difficult to eliminate any of our fits because of a discrepant $I(\mathrm{Ly}\alpha)/I(\mathrm{BaC})$ (the lowest $I(\mathrm{Ly}\alpha)/I(\mathrm{BaC})$ is 0.04, and the next lowest is 0.1), and the fact that we reproduce previous results to within an order of magnitude is encouraging given the limited range over which we can probe the Balmer continuum. Ultimately, comparisons to previous results for $I(\mathrm{Ly}\alpha)/I(\mathrm{BaC})$ do not reveal any glaring problems with our Balmer continuum fits.

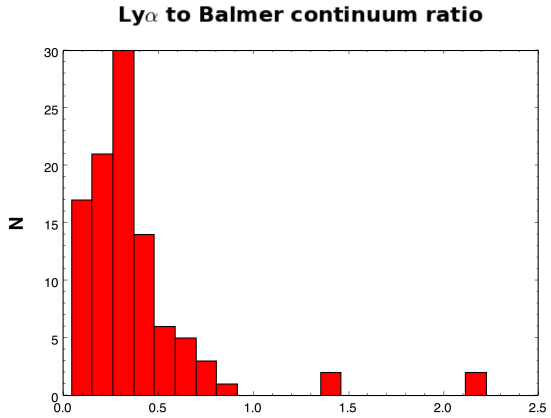

Fig. 12.— Distribution of $I(\mathrm{Ly}\alpha)/I(\mathrm{BaC})$ for 101 radio-loud and radio-quiet quasars with detectable Balmer continuum emission.

The dominant source of uncertainty arising from the Balmer continuum is the question of which model to use. Previous workers have used both optically thin (Jin et al. 2012) and optically thick Balmer continuum emission (Shen & Liu 2012). However, the optically thin and optically thick Balmer continua are extremely similar, especially on the blue edge of the Balmer continuum that we probe in this work. Instead, the largest source of uncertainty in our work comes from the electron temperature T_e, which sets the shape of the Balmer continuuum (see Figure 3 in Jin et al. 2012) and leads to large differences in Balmer continuum flux at $\lambda < 2500$ Å. Due to the difficulties inherent to fitting the Balmer

continuum, T_e is poorly constrained by observations. Previously workers typically either fix T_e at some value between 10000 and 20000 K (e.g. Denney et al. 2009; Shen & Liu 2012) or fit a grid of models with T_e varying over this range in relatively large steps (De Rosa et al. 2014). However, Tsuzuki et al. (2006) left T_e as a free parameter in their fits and managed to constraint it reasonably well. They find a mean T_e of 17000 K, with T_e for individual objects ranging between 7000 K and 37000 K (excluding one quasar with an anomalously large value of T_e of 200000 K). The electron temperature can also be obtained from analysis of the broad emission lines of hydrogen; using this method, Popović (2003) find T_e between 13000 and 37000 K, with some evidence that T_e decreases as Hβ FWHM increases (so our sample would be expected to have slightly lower T_e because the lines are quite broad). In conclusion, the range of possible electron temperatures for the Balmer continuum is quite large. Our fiducial value for T_e, 15000 K, while commonly used in previous work, does not appear to be especially favored by the data, and electron temperatures of 10000 and 20000 K appear to be just as well supported.

In order to obtain some understanding of the impact of the uncertainty in T_e, we re-run our fits with T_e set to 10000 and 20000 K. We find a median increase in mass of 0.12 decades when T_e is lowered to 10000 K, and a median decrease in mass of 0.12 decades when T_e is raised to 20000 K (Figure 13). However, the change in mass varies quite widely across the sample, essentially as a result of changes in Balmer continuum strength: if the Balmer continuum is very strong, the uncertainty due to T_e is much larger than if the Balmer continuum is weak. As a result, the rms mass difference is 0.36 decades when T_e is lowered to 10000 K, and 0.60 decades when T_e is raised to 20000 K. In conclusion, the uncertainty arising from T_e is sometimes quite large and varies from object to object; for the sample as a whole, it can estimated at 0.15–0.3 decades.

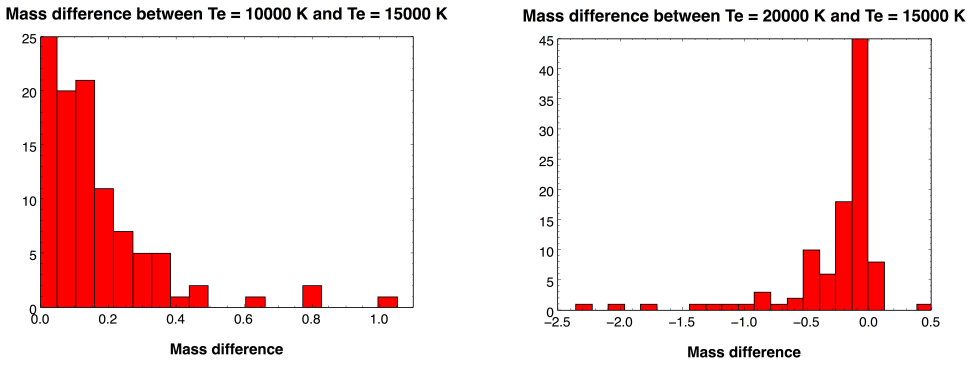

Fig. 13.— Distributions of the mass difference between (left) fits with T_e = 10000 K and fits with T_e = 15000 K; and (right) fits with T_e = 20000 K and fits with T_e = 15000 K. Plots only show the 102 quasars with measurable Balmer continua, out of the 141 quasars total. Two outliers are not plotted: a quasar with a difference of 2.78 decades between the mass at T_e = 10000 K and the mass at T_e = 15000 K, and a quasar with a difference of -3.40 decades between the mass at T_e = 20000 K and the mass at T_e = 15000 K.

5.7. Intrinsic reddening

Non-BAL Type I quasars are expected to have little dust extinction from the dusty torus responsible for blocking the broad line region in Type II quasars. Nevertheless, they may still exhibit some dust extinction from the quasar and the host galaxy, and even small amounts of reddening can have a significant effect on the rest-frame UV spectrum (Laor 1990). Krawczyk et al. (2014) find that the broad-line, non-BAL SDSS DR7 quasars exhibit little dust extinction, with 97.5% having $E(B-V) < 0.1$, and $\approx$ 70% having $E(B-V) < 0.03$. They also find that an SMC extinction law (Pei 1992) best fits the data, consistent with previous results (Hopkins et al. 2004) and with the absence of the 2200 Å absorption feature characteristic of Milky Way-like dust extinction. We assume that our sample of quasars follows the same reddening distribution as the entire sample of non-BAL SDSS quasars used in Krawczyk et al. (2014). Since our sample is substantially biased towards very high luminosities and redshifts compared to the SDSS quasar sample as a

whole, it is possible that the reddening distribution of our sample is substantially different than that of Krawczyk et al. (2014). However, it is not known how luminosity and redshift affect the distribution of intrinsic extinction, due to the difficulty in measuring $E(B-V)$ for individual quasars. Furthermore, it is possible that our radio loud sample will have different extinction properties than the SDSS sample as a whole: since radio loud quasars are oriented more nearly face on, they may have less dust extinction than other quasars. Again, however, lack of reliable estimates prevents us from using a more sophisticated estimate of the intrinsic reddening distribution.

In order to estimate the impact of dust reddening on our mass estimates, we apply an SMC-like extinction law with $E(B-V) = 0.005$, 0.018, 0.05, and 0.13 to each quasar in our sample and measure the change in mass. These extinctions correspond to the 50th, 68th, 90th, and 99th percentiles in the $E(B-V)$ distribution of Krawczyk et al. (2014). While these extinctions are quite small, they have a substantial effect on the mass estimates, leading to median mass differences of -0.05 decades for $E(B-V) = 0.005$, -0.24 decades for $E(B-V) = 0.018$, -2.46 decades for $E(B-V) = 0.05$, and -2.77 decades for $E(B-V) = 0.13$ (where the negative sign indicates that the dereddened spectra produce a lower mass estimate than the observed spectra). However, these values overstate the impact of intrinsic reddening. For many quasars, dereddening by $E(B-V) = 0.05$ or $E(B-V) = 0.13$ leads to unphysical fits, which explains why the impact of reddening plateaus at $E(B-V) = 0.13$. If, for some quasar, dereddening by some $E(B-V)$ leads to an unphysical accretion disk model fit, that means that we can rule out that value of $E(B-V)$. For $E(B-V) = 0.05$, the quasars with the largest change in mass (clustered on the left edge of the histogram) are also those quasars with unphysical fits, as T_{max} is nearly always at its upper boundary of 1 keV. This means that we should not consider these quasars when estimating the uncertainty associated with intrinsic reddening. For $E(B-V) = 0.05$, we should only consider the quasars with mass differences lying in the bell-shaped distribution around -0.5 decades, because these are the only quasars that could have $E(B-V) = 0.05$. Therefore, $E(B-V) = 0.05$ leads to a decrease in mass of 0.5

decades, not a decrease of 2.5 decades. For $E(B-V) = 0.13$, the situation is worse because almost every fit has $T_{max} = 1$ keV; for only a few quasars is such an extreme reddening allowed, exactly in line with the distribution of Krawczyk et al. (2014).

The dramatic impact of reddening on mass is primarily due to its modification of the spectral shape: higher frequencies are reddened more than lower frequencies, shifting the spectral peak towards the red and thus leading to an overestimate of the mass if the intrinsic reddening is not corrected. As a result, mass is both somewhat overestimated on average and fairly uncertain due to the uncertainty in determining $E(B-V)$ for individual sources. The magnitude of the bias is probably 0.1–0.2 decades, and the uncertainty from intrinsic reddening is probably 0.2–0.3 decades.

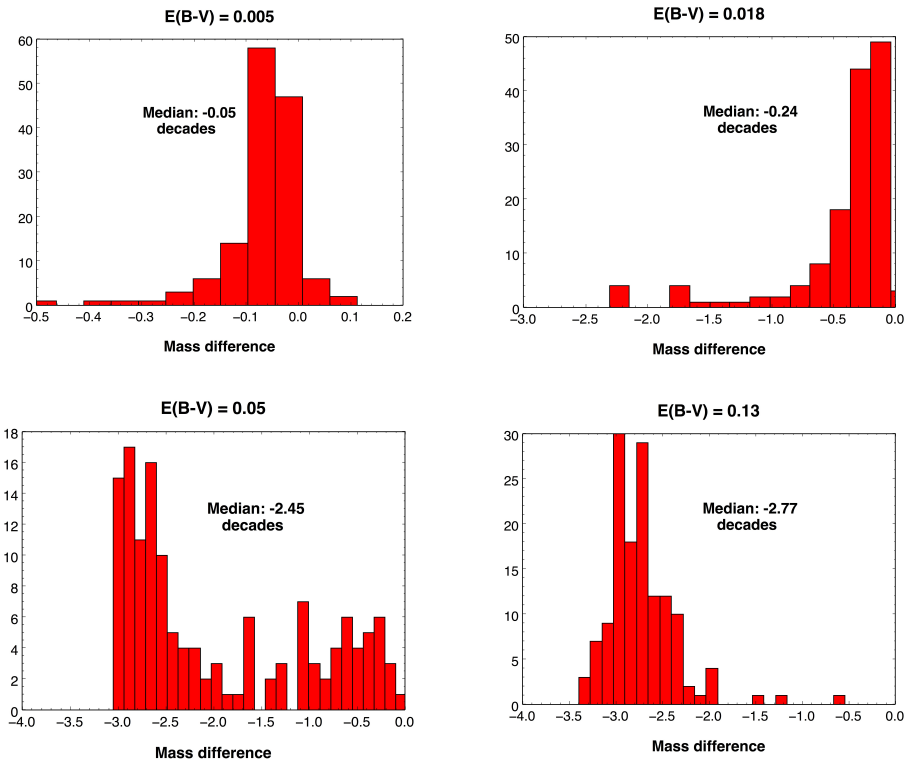

Fig. 14.— Distributions of the mass difference when intrinsic reddening is corrected using different values of $E(B-V)$. To better display the histograms, we do not show several outliers in mass difference: three outliers at -1.14, 0.54, and 2.52 decades mass difference for $E(B-V) = 0.005$; two outliers at 0.58 and 2.55 decades mass difference for $E(B-V) = 0.018$; two outliers at 0.68 and 2.63 decades mass difference for $E(B-V) = 0.05$; and two outliers at 0.86 and 2.5 decades mass difference for $E(B-V) = 0.13$.

6. Results and Discussion

Using the methods described in the previous section, we determine the accretion disk model masses and their statistical errors for 67 radio loud quasars and 74 radio quiet quasars with acceptable, physical fits (Table 3 and Table 4). These masses assume $1/\sqrt{\cos i} = 1.15$ and $f_{\rm col}$ calculated using the fitted temperature profile and Equation 18. Systematic errors are not reported in Table 3 and Table 4.

Table 3.

SDSS ID	z	$M_i(z=2)$	Total 1.4 GHz flux (mJy)	Core 1.4 GHz flux (mJy)	Mass $\log(M_\odot)$
084715.16+383109.9	3.19	-28.55	381	374	
153514.65+483659.7	2.56	-28.58	578	26	$9.27^{+0.01}_{-0.03}$
153514.65+483659.7	2.56	-28.58	578	26	$9.05^{+0.41}_{-0.06}$
153514.65+483659.7	2.56	-28.58	578	26	$9.15^{+0.06}_{-0.04}$
140501.12+041535.8	3.21	-27.57	52	52	
074625.87+254902.1	2.99	-27.33	428	428	
153514.65+483659.7	2.56	-28.58	578	26	$8.97^{+0.04}_{-0.04}$
153514.65+483659.7	2.56	-28.58	578	26	$9.43^{+0.05}_{-0.05}$
153514.65+483659.7	2.56	-28.58	578	26	$9.56^{+0.03}_{-0.01}$
153514.65+483659.7	2.56	-28.58	578	26	$9.30^{+0.02}_{-0.02}$
153514.65+483659.7	2.56	-28.58	578	26	$9.42^{+0.02}_{-0.02}$
153514.65+483659.7	2.56	-28.58	578	26	$9.54^{+0.01}_{-0.01}$
082428.02+234107.9	2.61	-27.74	530	326	
080100.48+115323.5	2.67	-27.34	91	91	
153514.65+483659.7	2.56	-28.58	578	26	$9.37^{+0.08}_{-0.09}$
153514.65+483659.7	2.56	-28.58	578	26	$9.67^{+0.00}_{-0.01}$
153514.65+483659.7	2.56	-28.58	578	26	$8.97^{+0.09}_{-0.15}$
153514.65+483659.7	2.56	-28.58	578	26	$8.28^{+0.14}_{-0.21}$
153514.65+483659.7	2.56	-28.58	578	26	$9.18^{+0.03}_{-0.03}$
153514.65+483659.7	2.56	-28.58	578	26	$8.99^{+0.06}_{-0.05}$
153514.65+483659.7	2.56	-28.58	578	26	$9.52^{+0.01}_{-0.02}$
153514.65+483659.7	2.56	-28.58	578	26	$9.48^{+0.01}_{-0.01}$
153514.65+483659.7	2.56	-28.58	578	26	$9.25^{+0.01}_{-0.04}$
153514.65+483659.7	2.56	-28.58	578	26	$9.47^{+0.01}_{-0.02}$
153514.65+483659.7	2.56	-28.58	578	26	$9.11^{+0.04}_{-0.05}$
153514.65+483659.7	2.56	-28.58	578	26	$8.75^{+0.08}_{-0.16}$
121548.91+642228.4	3.24	-28.33	121	121	
141318.86+450523.0	3.12	-27.71	291	88	
153514.65+483659.7	2.56	-28.58	578	26	$8.66^{+0.05}_{-0.07}$
153514.65+483659.7	2.56	-28.58	578	26	$9.06^{+0.05}_{-0.04}$
153514.65+483659.7	2.56	-28.58	578	26	$9.03^{+0.02}_{-0.04}$
153514.65+483659.7	2.56	-28.58	578	26	$8.86^{+0.05}_{-0.06}$
142950.91+260750.2	2.91	-28.56	78	33	

Table 3—Continued

SDSS ID	z	$M_i(z=2)$	Total 1.4 GHz flux (mJy)	Core 1.4 GHz flux (mJy)	Mass $\log(M_\odot)$
153514.65+483659.7	2.56	-28.58	578	26	$9.14^{+0.02}_{-0.02}$
153514.65+483659.7	2.56	-28.58	578	26	
153514.65+483659.7	2.56	-28.58	578	26	$9.20^{+0.04}_{-0.02}$
153514.65+483659.7	2.56	-28.58	578	26	$9.70^{+0.02}_{-0.02}$
153514.65+483659.7	2.56	-28.58	578	26	$8.68^{+0.10}_{-0.16}$
153514.65+483659.7	2.56	-28.58	578	26	$9.24^{+0.01}_{-0.01}$
153514.65+483659.7	2.56	-28.58	578	26	$8.84^{+0.08}_{-0.10}$
153514.65+483659.7	2.56	-28.58	578	26	$9.34^{+0.03}_{-0.02}$
094442.31+255443.3	2.92	-28.30	457	457	
153514.65+483659.7	2.56	-28.58	578	26	$8.76^{+0.07}_{-0.05}$
153514.65+483659.7	2.56	-28.58	578	26	$9.19^{+0.08}_{-0.08}$
124209.81+372005.6	3.83	-27.91	110	87	
153514.65+483659.7	2.56	-28.58	578	26	$9.47^{+0.07}_{-0.08}$
153514.65+483659.7	2.56	-28.58	578	26	$8.84^{+0.06}_{-0.05}$
133724.69+315254.5	3.18	-28.41	55	47	
093447.23+305055.7	2.89	-26.25	188	188	
153514.65+483659.7	2.56	-28.58	578	26	$9.06^{+0.02}_{-0.03}$
153514.65+483659.7	2.56	-28.58	578	26	$9.28^{+0.04}_{-0.06}$
153514.65+483659.7	2.56	-28.58	578	26	$9.78^{+0.02}_{-0.05}$
153514.65+483659.7	2.56	-28.58	578	26	$7.54^{+0.90}_{-1.65}$
153514.65+483659.7	2.56	-28.58	578	26	$8.36^{+0.12}_{-0.19}$
153514.65+483659.7	2.56	-28.58	578	26	$9.36^{+0.03}_{-0.02}$
153514.65+483659.7	2.56	-28.58	578	26	$8.77^{+0.09}_{-0.15}$
153514.65+483659.7	2.56	-28.58	578	26	$9.35^{+0.03}_{-0.01}$
153514.65+483659.7	2.56	-28.58	578	26	$9.23^{+0.03}_{-0.02}$
153514.65+483659.7	2.56	-28.58	578	26	$8.62^{+0.07}_{-0.09}$
153514.65+483659.7	2.56	-28.58	578	26	$7.48^{+0.58}_{-1.22}$
153514.65+483659.7	2.56	-28.58	578	26	$9.31^{+0.01}_{-0.04}$
153514.65+483659.7	2.56	-28.58	578	26	$8.64^{+0.06}_{-0.08}$
100741.50+135629.6	2.71	-28.11	412	412	
153514.65+483659.7	2.56	-28.58	578	26	$9.69^{+0.02}_{-0.01}$
142921.87+540611.1	3.01	-26.90	816	799	
153514.65+483659.7	2.56	-28.58	578	26	$9.39^{+0.01}_{-0.01}$

Table 3—Continued

SDSS ID	z	$M_i(z=2)$	Total 1.4 GHz flux (mJy)	Core 1.4 GHz flux (mJy)	Mass $\log(M_\odot)$
153514.65+483659.7	2.56	-28.58	578	26	$9.16^{+0.02}_{-0.02}$
153514.65+483659.7	2.56	-28.58	578	26	$9.48^{+0.01}_{-0.02}$
135326.02+572552.8	3.47	-27.74	214	214	
140653.84+343337.3	2.56	-27.93	124	124	
113017.37+073212.9	2.66	-29.39	74	74	
153514.65+483659.7	2.56	-28.58	578	26	$9.36^{+0.01}_{-0.01}$
122343.15+503753.4	3.50	-29.65	66	66	
153514.65+483659.7	2.56	-28.58	578	26	$9.71^{+0.00}_{-0.00}$
153514.65+483659.7	2.56	-28.58	578	26	$9.44^{+0.03}_{-0.06}$
153514.65+483659.7	2.56	-28.58	578	26	$9.52^{+0.01}_{-0.01}$
153514.65+483659.7	2.56	-28.58	578	26	$9.06^{+0.06}_{-0.05}$
153514.65+483659.7	2.56	-28.58	578	26	$10.15^{+0.06}_{-0.02}$
153514.65+483659.7	2.56	-28.58	578	26	$8.83^{+0.05}_{-0.08}$
153514.65+483659.7	2.56	-28.58	578	26	$9.39^{+0.06}_{-0.04}$
153514.65+483659.7	2.56	-28.58	578	26	$9.14^{+0.03}_{-0.07}$
153514.65+483659.7	2.56	-28.58	578	26	$9.36^{+0.02}_{-0.04}$
153514.65+483659.7	2.56	-28.58	578	26	$8.85^{+0.03}_{-0.05}$
153514.65+483659.7	2.56	-28.58	578	26	$9.24^{+0.04}_{-0.02}$
153514.65+483659.7	2.56	-28.58	578	26	$9.34^{+0.02}_{-0.01}$
153514.65+483659.7	2.56	-28.58	578	26	$9.44^{+0.02}_{-0.02}$

Note. — The sample of 86 radio-loud quasars.

Table 4.

SDSS ID	z	$M_i(z=2)$	Mass ($\log(M_\odot)$)
094114.38+213851.7	2.58	-28.62	$9.28^{+0.03}_{-0.02}$
094114.38+213851.7	2.58	-28.62	
094114.38+213851.7	2.58	-28.62	$9.36^{+0.04}_{-0.03}$
094114.38+213851.7	2.58	-28.62	$9.78^{+0.01}_{-0.00}$
094114.38+213851.7	2.58	-28.62	$9.19^{+0.02}_{-0.03}$
094114.38+213851.7	2.58	-28.62	$8.91^{+0.05}_{-0.05}$
094114.38+213851.7	2.58	-28.62	$9.21^{+0.01}_{-0.01}$
101549.00+002020.0	4.41	-28.50	
094114.38+213851.7	2.58	-28.62	$9.18^{+0.02}_{-0.02}$
094114.38+213851.7	2.58	-28.62	$9.12^{+0.02}_{-0.04}$
094114.38+213851.7	2.58	-28.62	$9.23^{+0.01}_{-0.01}$
094114.38+213851.7	2.58	-28.62	$9.60^{+0.01}_{-0.01}$
094114.38+213851.7	2.58	-28.62	$8.70^{+0.03}_{-0.05}$
094114.38+213851.7	2.58	-28.62	$8.54^{+0.06}_{-0.06}$
001134.52+155137.4	4.31	-27.69	
094114.38+213851.7	2.58	-28.62	$9.03^{+0.01}_{-0.02}$
094114.38+213851.7	2.58	-28.62	$8.42^{+0.09}_{-0.15}$
085309.70+232454.3	2.54	-27.45	
094114.38+213851.7	2.58	-28.62	$9.18^{+0.03}_{-0.01}$
094114.38+213851.7	2.58	-28.62	$8.93^{+0.07}_{-0.07}$
094114.38+213851.7	2.58	-28.62	$9.02^{+0.02}_{-0.04}$
101336.37+561536.3	3.65	-28.94	
094114.38+213851.7	2.58	-28.62	$9.42^{+0.01}_{-0.04}$
094114.38+213851.7	2.58	-28.62	$9.30^{+0.01}_{-0.02}$
094114.38+213851.7	2.58	-28.62	$8.59^{+0.06}_{-0.09}$
094114.38+213851.7	2.58	-28.62	$8.64^{+0.06}_{-0.00}$
130833.48+362622.1	3.23	-28.42	
094114.38+213851.7	2.58	-28.62	$9.02^{+0.02}_{-0.04}$
094114.38+213851.7	2.58	-28.62	$8.99^{+0.02}_{-0.01}$
094114.38+213851.7	2.58	-28.62	$9.54^{+0.01}_{-0.01}$
090218.51+050317.5	2.97	-27.71	
155716.40+080213.6	3.05	-27.59	
150955.64+270932.9	2.91	-28.61	
094114.38+213851.7	2.58	-28.62	$8.71^{+0.06}_{-0.05}$

Table 4—Continued

SDSS ID	z	$M_i(z=2)$	Mass ($\log(M_\odot)$)
094114.38+213851.7	2.58	-28.62	$8.80^{+0.05}_{-0.07}$
094114.38+213851.7	2.58	-28.62	$8.95^{+0.03}_{-0.01}$
094114.38+213851.7	2.58	-28.62	$8.80^{+0.02}_{-0.04}$
094114.38+213851.7	2.58	-28.62	$8.70^{+0.04}_{-0.05}$
094114.38+213851.7	2.58	-28.62	$8.98^{+0.05}_{-0.04}$
094114.38+213851.7	2.58	-28.62	$8.85^{+0.03}_{-0.04}$
094114.38+213851.7	2.58	-28.62	$9.14^{+0.02}_{-0.04}$
094114.38+213851.7	2.58	-28.62	$9.28^{+0.01}_{-0.01}$
094114.38+213851.7	2.58	-28.62	$8.76^{+0.02}_{-0.03}$
094114.38+213851.7	2.58	-28.62	$8.50^{+0.12}_{-0.20}$
094114.38+213851.7	2.58	-28.62	$8.75^{+0.08}_{-0.11}$
094114.38+213851.7	2.58	-28.62	$8.44^{+0.08}_{-0.15}$
094114.38+213851.7	2.58	-28.62	$9.02^{+0.02}_{-0.04}$
094114.38+213851.7	2.58	-28.62	$9.49^{+0.01}_{-0.01}$
094114.38+213851.7	2.58	-28.62	$8.98^{+0.01}_{-0.01}$
094114.38+213851.7	2.58	-28.62	$8.76^{+0.04}_{-0.02}$
094114.38+213851.7	2.58	-28.62	$8.90^{+0.04}_{-0.04}$
094114.38+213851.7	2.58	-28.62	$9.22^{+0.02}_{-0.05}$
094114.38+213851.7	2.58	-28.62	$8.48^{+0.06}_{-0.10}$
101008.45+280918.3	3.20	-27.55	
094114.38+213851.7	2.58	-28.62	$8.41^{+0.06}_{-0.10}$
094114.38+213851.7	2.58	-28.62	$9.37^{+0.04}_{-0.05}$
094114.38+213851.7	2.58	-28.62	$9.43^{+0.01}_{-0.01}$
094114.38+213851.7	2.58	-28.62	$9.18^{+0.03}_{-0.02}$
094114.38+213851.7	2.58	-28.62	$8.54^{+0.04}_{-0.04}$
094114.38+213851.7	2.58	-28.62	$8.25^{+0.07}_{-0.08}$
094114.38+213851.7	2.58	-28.62	$9.30^{+0.01}_{-0.03}$
094114.38+213851.7	2.58	-28.62	$8.05^{+0.37}_{-0.17}$
094114.38+213851.7	2.58	-28.62	$9.20^{+0.01}_{-0.02}$
094114.38+213851.7	2.58	-28.62	$9.58^{+0.00}_{-0.00}$
094114.38+213851.7	2.58	-28.62	$8.92^{+0.05}_{-0.06}$
094114.38+213851.7	2.58	-28.62	$9.29^{+0.03}_{-0.01}$
094114.38+213851.7	2.58	-28.62	$8.70^{+0.06}_{-0.06}$
094114.38+213851.7	2.58	-28.62	$9.11^{+0.01}_{-0.01}$

6.1. Eddington ratios

We compute Eddington luminosities using the black hole mass from the accretion disk fit and Eddington ratios using the estimated bolometric luminosity from the Shen et al. (2011) catalog (Figure 15). Both the radio loud and radio quiet samples exhibit a range of Eddington ratios, and both have a substantial number of quasars (23 radio loud, 33 radio quiet) with Eddington ratios greater than 1. Since we consider the most luminous subset of quasars, it is not implausible that some of these quasars are indeed accreting at super-Eddington rates. However, another possibility is that our masses are biased low. The two systematic effects that can bias our mass estimates are the spin of the black hole and the intrinsic reddening (which will always lead to lower black hole masses). If the average quasar has $a_* \approx 1$, then the masses will be biased low by 0.4 decades if there is no intrinsic reddening, and 0.1–0.2 decades with modest intrinsic reddening. This can explain some but not all of the super-Eddington ratios, since in the most extreme case the bolometric luminosity exceeds the Eddington luminosity by 0.7 decades.

Table 4—Continued

SDSS ID	z	$M_i(z=2)$	Mass ($\log(M_\odot)$)
094114.38+213851.7	2.58	-28.62	$9.67^{+0.02}_{-0.02}$
092917.31+052302.2	2.55	-27.97	
094114.38+213851.7	2.58	-28.62	$9.19^{+0.01}_{-0.01}$
094114.38+213851.7	2.58	-28.62	$9.81^{+0.01}_{-0.00}$
094114.38+213851.7	2.58	-28.62	$9.35^{+0.01}_{-0.01}$
094114.38+213851.7	2.58	-28.62	$9.14^{+0.03}_{-0.04}$
094114.38+213851.7	2.58	-28.62	$9.30^{+0.02}_{-0.01}$
094114.38+213851.7	2.58	-28.62	$9.42^{+0.01}_{-0.05}$
094114.38+213851.7	2.58	-28.62	$8.69^{+0.08}_{-0.14}$
094114.38+213851.7	2.58	-28.62	$9.16^{+0.04}_{-0.06}$
094114.38+213851.7	2.58	-28.62	$8.77^{+0.03}_{-0.05}$
094114.38+213851.7	2.58	-28.62	$8.96^{+0.07}_{-0.07}$
094114.38+213851.7	2.58	-28.62	$8.61^{+0.10}_{-0.21}$
094114.38+213851.7	2.58	-28.62	$9.05^{+0.06}_{-0.04}$
094114.38+213851.7	2.58	-28.62	$9.10^{+0.03}_{-0.02}$
094114.38+213851.7	2.58	-28.62	$9.22^{+0.02}_{-0.02}$
094114.38+213851.7	2.58	-28.62	$9.13^{+0.01}_{-0.01}$
094114.38+213851.7	2.58	-28.62	

Note. — The matched sample of 86 radio-quiet quasars.

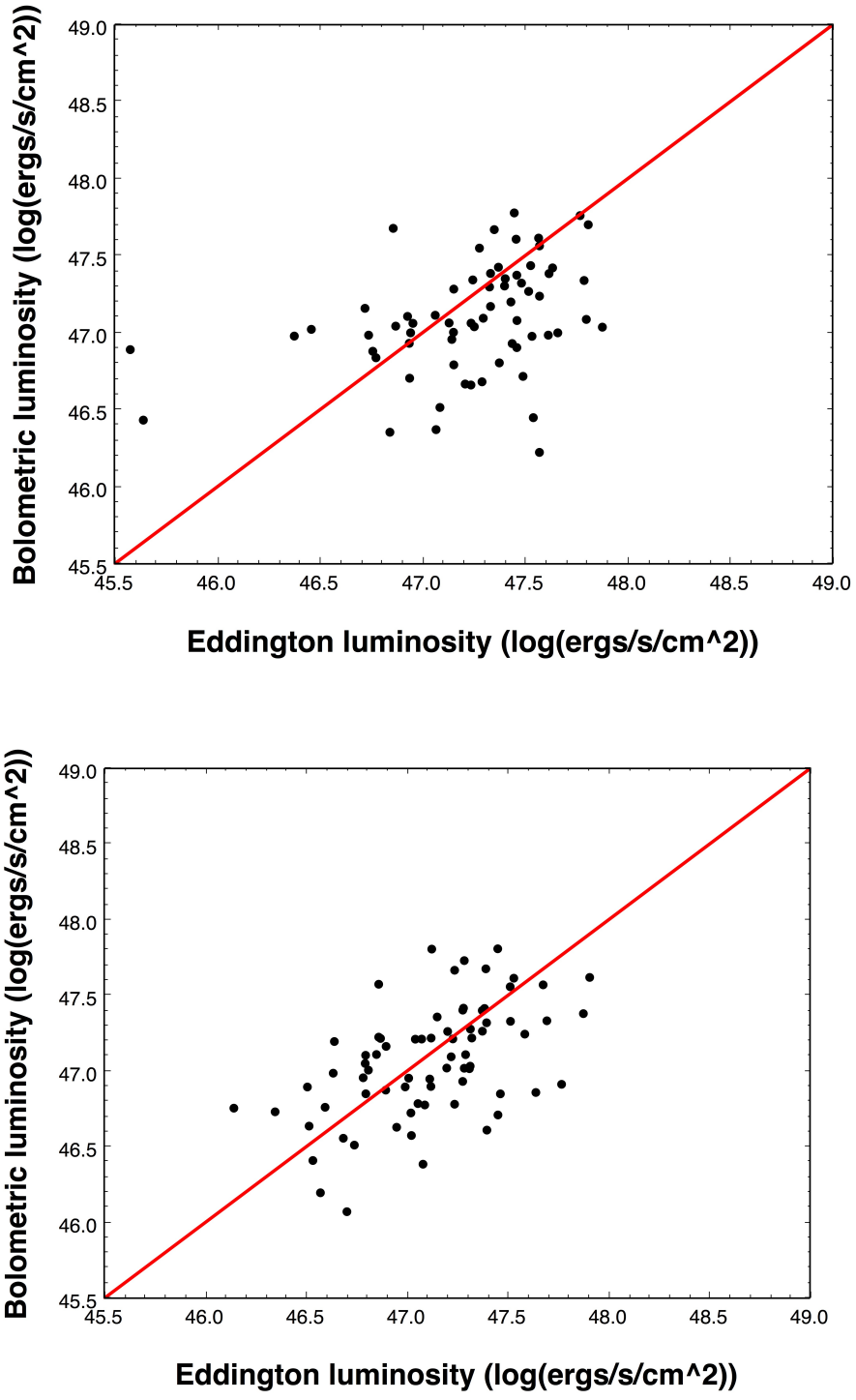

Fig. 15.— Comparison between bolometric and Eddington luminosity for radio loud (top) and radio quiet (bottom) samples. Red line indicates an Eddington ratio of 1.

The high observed Eddington ratios also indicate that thin disk models may be inappropriate. Thin disk models are inconsistent at accretion rates greater than 30% of the Eddington accretion rate, since at higher accretion rates radiation pressure significantly affects the gas motion, violating the assumption of geometrical thinness (Laor & Netzer 1989). At accretion rates comparable to the Eddington accretion rate, the accretion flow assumes a "slim disk" geometry instead (Abramowicz et al. 1988). Spectra have been computed for slim disk models, although no models exist to fit slim disks to spectral data. These models show that slim disk spectra are very similar to thin disk spectra for accretion rates below the Eddington rate, but as the accretion rate increases above the Eddington rate, the flux from the slim disk spectra decreases, although the shape does not change (Szuszkiewicz et al. 1996; Mineshige et al. 2000). At very high accretion rates (100-1000 times Eddington), however, the slim disk spectrum becomes substantially flatter than the thin disk spectrum (Mineshige et al. 2000).

Most of our super-Eddington quasars have luminosities just slightly above the Eddington luminosity. As a result, the modeled disk luminosity is overestimated by up to ≈ 0.5 decades (as estimated from Figure 10b in (Szuszkiewicz et al. 1996)), and therefore masses are underestimated by ≈ 0.2 decades. If the black hole also has $a_* \approx 1$, then a substantially smaller fraction of quasars have super-Eddington luminosities than reported above, and a thin disk model does in fact accurately describe the shape of the spectrum (if suitably scaled at modestly super-Eddington luminosities to account for the lower efficiency of slim disks). Thus, fitting thin disk models to the spectra, while technically inconsistent, would not actually lead to substantial additional errors in the mass estimates. However, we cannot exclude the possibility that some of the quasars in our sample have very large accretion rates, since the luminosity-accretion rate relationship plateaus at luminosities more than a factor of a few greater than Eddington (Szuszkiewicz et al. 1996; Mineshige et al. 2000). If this is the case, then fitting thin accretion disk models is manifestly incorrect, because the shape of the true emitted spectrum deviates substantially from the thin disk spectrum.

6.2. Comparison to virial masses

We compare the accretion disk masses to the virial masses from the Shen et al. (2011) catalog (Figure 16). First, the disk masses and virial masses correlate with each other. For the entire sample of 141 quasars, the Pearson correlation coefficient between the disk masses is 0.33, with a p-value of 8.3×10^{-5}. The situation is similar for the radio quiet quasars, which have $r = 0.57$ and $p = 1.4 \times 10^{-7}$ for the relationship between the virial masses and the disk masses. For the radio loud quasars, however, the situation is somewhat different: the correlation coefficient is only 0.2, with $p = 0.11$. This result is not merely an artifact of outliers: if we remove the two radio-loud quasars with $M \approx 10^8 M_\odot$, which also have very high $T_{\rm max}$ and large residuals between the virial masses and the disk masses, the correlation coefficient and p value are mostly unchanged, at 0.22 and 0.08 respectively. If the masses are adjusted to have the same means, the rms scatter between disk and virial masses for the radio quiet quasars is 0.40 decades, while the rms scatter between the disk and virial masses for the radio loud quasars is 0.60 decades.

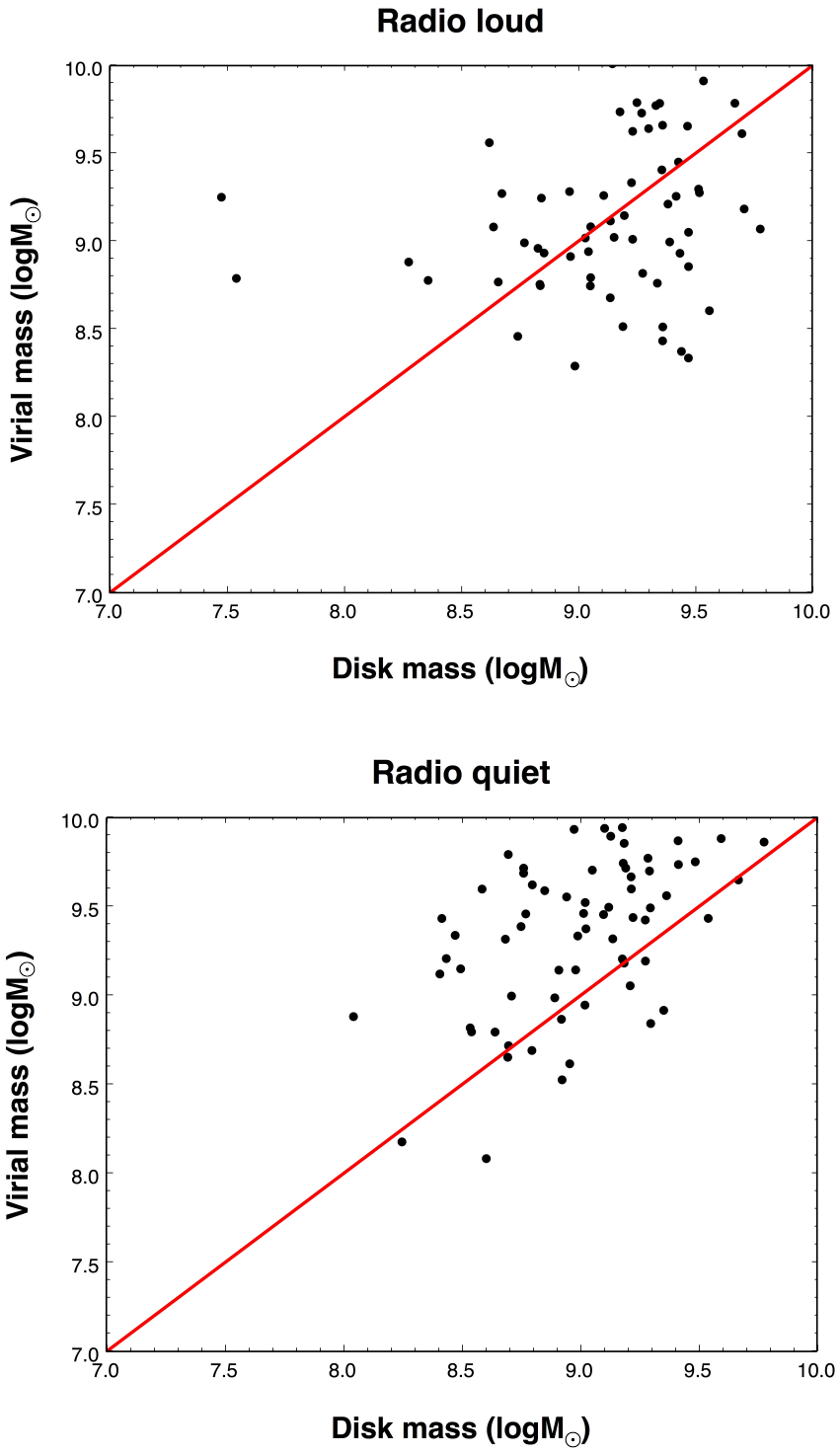

Fig. 16.— Comparison between the Shen et al. (2011) virial masses and the disk masses for the radio loud sample (top) and the radio quiet sample (bottom).

The disk masses and virial masses are also offset, although the offset is different for the radio loud and radio quiet quasars. The median radio loud disk mass (9.23 $\log(M_\odot)$) is greater than the median radio loud virial mass (9.09 $\log(M_\odot)$); with standard errors of ≈ 0.05 decades for both the disk and virial masses, this is a 2 σ difference. The offset between the disk and virial masses is much more significant for the radio quiet quasars: the median disk mass (9.03 $\log(M_\odot)$) is substantially smaller than the median virial mass (9.46 $\log(M_\odot)$). This difference is significant at greater than 5 σ.

We take the agreement between the radio quiet disk masses and virial masses as an indication that they both reflect the true masses of the quasars. While both the virial masses and the disk masses possess substantial overall uncertainties, it would be quite unlikely for the relationship between them to arise solely due to chance, suggesting that they are both measuring the same quantity. In contrast, the large scatter and lack of agreement between the disk masses and the virial masses for the radio loud sample suggests that one or both of the mass estimators is substantially contaminated by a systematic effect unique to the radio loud sample. It is possible that the continuum emission of the radio loud quasars is substantially contaminated by optical/ultraviolet synchrotron emission (Whiting et al. 2001). In this case, both the virial masses and the disk masses would show increased errors, as the continum emission would no longer originate solely from the disk, and the monochromatic 1350 Å luminosity would no longer be tightly related to the extreme ultraviolet ionizing continuum. However, the synchrotron explanation is inconsistent with the offset between the virial and disk masses: an unsubtracted synchrotron component would cause the spectra to be redder, making the maximum temperature lower and leading to overestimates in the disk mass rather than underestimates. It is also possible that the increased scatter is due to increasingly problematic virial masses for the radio-loud quasars: radio-loud quasars may have more prominent outflows, increasing the scatter between the virial velocity and the line width and thus increasing the uncertainty of the virial masses. Properly understanding this relationship will require larger samples of radio-loud and radio-quiet quasars in order to reduce statistical uncertainties.

6.3. CIV or disk masses?

Using the error estimates from Section 5, we compute the total error budget for the accretion disk masses (Table 5). We estimate that the total error on the accretion disk masses is ≈ 0.45 decades on average. However, this number conceals large variations in error between sources. For instance, the uncertainty on the Lyα forest correction is substantially higher for high redshift quasars, but the uncertainty of the Balmer continuum is lower, as the Balmer continuum is redshifted out of the wavelength coverage at sufficiently high redshift. Similarly, if the spin of $M > 10^9 M_\odot$ quasars is confirmed to be $a_* = 1$ in all cases, the uncertainty from spin will be significantly lower for these quasars.

Our error estimate for the accretion disk models is similar to error estimates for the CIV-based virial masses. However, the 0.4 decade scatter between the disk masses and the CIV masses for the radio quiet quasars is considerably lower than either estimate (note that we disregard the radio loud sample in this section, since the lack of correlation between radio loud disk masses and virial masses suggests radio loud quasars are affected by a systematic effect not considered in Section 5). Since the virial masses and accretion disk masses are based on radically different approaches, we expect most of their mass error to be uncorrelated; thus, the scatter between them should be the sum in quadrature of the disk mass error and the virial mass error. This discrepancy suggests that the uncertainties of the disk masses and the virial masses may be overestimated. However, more data are needed to confirm the 0.4 decade scatter between the CIV masses and the disk masses.

Given this analysis, which mass estimate should be preferred? The error analysis is inconclusive, as the uncertainties in the disk masses and the virial masses are about the same. The greater simplicity of the virial masses and the wealth of previous studies on CIV based masses are points in their favor. However, it is possible that it will prove too difficult to squeeze out virial velocity information from CIV line profiles, especially for large survey data which is necessarily limited to fairly low signal-to-noise ratios (e.g. SDSS and BOSS, which are by far the largest collections of quasar spectra available today). As a result, in

the future the CIV masses may be limited to similar accuracies as today. On the other hand, the accretion disk models can be improved substantially with better information about intrinsic reddening and black hole spin, both of which are achievable in the near future due to measurements enabled by large samples of quasars (e.g. Krawczyk et al. 2014). Moreover, accretion disk mass estimates provide an absolute mass scale, while virial masses must be calibrated to results from reverberation mapping, which are ultimately calibrated using the local $M - \sigma$ relationship. Accretion disk models could therefore be used to calibrate virial masses at high redshift. Ultimately, however, further tests are needed of the agreement between accretion disk masses and the high-quality masses available from reverberation mapping; without such tests, it is difficult to determine the accuracy of the disk masses.

Table 5.

Name	Magnitude
Fitting errors	0.05
SDSS flux calibration	0.02
Inclination	0.12
Spin	0.2
Lyα forest correction	0.12
Balmer continuum	0.2
Intrinsic reddening	0.3
Total	0.45

Note. — Total error budget for the accretion disk masses

7. Conclusions and Future Directions

In this thesis I present several new results and tools applicable for determining quasar masses by fitting accretion disk models:

1. I present a tool for fitting accretion disk models to $z > 2.5$ quasars, including estimation of the uncertainty on the mass.

2. More significantly, this tool can also be used to better understand systematic errors in the accretion disk mass measurements. I present rough estimates of the contributions from different sources of error; the major sources of error are the intrinsic reddening, shape of the Balmer continuum, and the spin of the black hole. With these major sources of error identified, more comprehensive modeling can better determine the contributions of each source to the overall uncertainty.

3. I compare the accretion disk masses to virial masses from the CIV line. I find that for radio quiet quasars, the accretion disk masses agree well with the virial masses, but that the relationship is considerably less strong for radio loud quasars, possibly due to an unidentified systematic error in either the disk masses or the virial masses of radio loud quasars. However, comparisons of the overall error budget for accretion disk masses and for virial masses are inconclusive, and comparisons to the CIV masses alone are insufficient in establishing the accuracy of the accretion disk masses due to the large scatter in the CIV masses. Therefore, it is unclear whether the disk masses are more accurate than the CIV virial masses.

There is much work to be done to better understand the impact of systematic errors on quasar mass estimates from accretion disks. We have presented the most significant sources of error (intrinsic reddening, spin, Balmer continuum), but a more comprehensive analysis is needed to more precisely determine their overall contributions to the error budget. Additionally, the accuracy of the disk masses can be better determined by comparing them to more accurately determined masses, including:

1. Larger sample sizes to determine the differences between disk and virial masses for both radio loud and radio quiet quasars. The results of Section 6.2 are intriguing, but without more data, it is hard to determine how significant they are.

2. Comparison between accretion disk masses and virial masses for $z > 2.5$ quasars with virial masses determined from infrared spectroscopy of Hβ or MgII. Since these are more reliable mass estimates than the CIV virial masses used here, comparison with them would give better information on the accuracy of the accretion disk masses.

3. Repeated fits of the accretion disk model to quasars with spectra at multiple epochs, similar to the tests performed on virial masses in Shen (2013) and Wilhite et al. (2007). The effect of variability on the mass estimates will give us a better idea of their overall uncertainty.

4. Comparison between accretion disk masses and reverberation mapping masses from the upcoming SDSS-RM project. SDSS-RM is a reverberation mapping project targeting a large number of high-redshift quasars, including quasars at $z \approx 3$. The highest redshift quasars in this sample will be ideal for comparison with accretion disk masses, since accretion disk masses for these quasars will suffer from the same systematic errors as for our sample.

Finally, use of broader band photometry can help better constrain the accretion disk masses. Ultimately, the continuum contains considerably more data with the lines; but continuum fitting requires considerably more care in order to accurately disentangle the quasar SED.

REFERENCES

Abramowicz, M. A. 2009, A&A, 500, 213

Abramowicz, M. A., Czerny, B., Lasota, J. P., & Szuszkiewicz, E. 1988, ApJ, 332, 646

Adelman-McCarthy, J. K., Agüeros, M. A., Allam, S. S., et al. 2008, ApJS, 175, 297

Assef, R. J., Denney, K. D., Kochanek, C. S., et al. 2011, ApJ, 742, 93

Baskin, A., & Laor, A. 2005, MNRAS, 356, 1029

Becker, R. H., White, R. L., & Helfand, D. J. 1995, ApJ, 450, 559

Bentz, M. C., & Katz, S. 2015, PASP, 127, 67

Bentz, M. C., Peterson, B. M., Netzer, H., Pogge, R. W., & Vestergaard, M. 2009, ApJ, 697, 160

Blandford, R. D., & McKee, C. F. 1982, ApJ, 255, 419

Blanton, M. R., Lin, H., Lupton, R. H., et al. 2003, AJ, 125, 2276

Calderone, G., Ghisellini, G., Colpi, M., & Dotti, M. 2013, MNRAS, 431, 210

Capellupo, D. M., Netzer, H., Lira, P., Trakhtenbrot, B., & Mejía-Restrepo, J. 2015, MNRAS, 446, 3427

Cardelli, J. A., Clayton, G. C., & Mathis, J. S. 1989, ApJ, 345, 245

Castignani, G., Haardt, F., Lapi, A., et al. 2013, A&A, 560, A28

Davis, S. W., Done, C., & Blaes, O. M. 2006, ApJ, 647, 525

Davis, S. W., Woo, J.-H., & Blaes, O. M. 2007, ApJ, 668, 682

De Rosa, G., Venemans, B. P., Decarli, R., et al. 2014, ApJ, 790, 145

Denney, K. D. 2012, ApJ, 759, 44

Denney, K. D., Peterson, B. M., Dietrich, M., Vestergaard, M., & Bentz, M. C. 2009, ApJ, 692, 246

Denney, K. D., Pogge, R. W., Assef, R. J., et al. 2013, ApJ, 775, 60

Done, C., Davis, S. W., Jin, C., Blaes, O., & Ward, M. 2012, MNRAS, 420, 1848

Faucher-Giguère, C.-A., Prochaska, J. X., Lidz, A., Hernquist, L., & Zaldarriaga, M. 2008, ApJ, 681, 831

Fine, S., Croom, S. M., Bland-Hawthorn, J., et al. 2010, MNRAS, 409, 591

Frank, J., King, A., & Raine, D. 1992, Accretion power in astrophysics.

Freeman, P., Doe, S., & Siemiginowska, A. 2001, in Society of Photo-Optical Instrumentation Engineers (SPIE) Conference Series, Vol. 4477, Astronomical Data Analysis, ed. J.-L. Starck & F. D. Murtagh, 76–87

Fukugita, M., Ichikawa, T., Gunn, J. E., et al. 1996, AJ, 111, 1748

Gabor, J. M., Impey, C. D., Jahnke, K., et al. 2009, ApJ, 691, 705

Ghisellini, G., Della Ceca, R., Volonteri, M., et al. 2010, MNRAS, 405, 387

Gierliński, M., Zdziarski, A. A., Poutanen, J., et al. 1999, MNRAS, 309, 496

Gobeille, D. B., Wardle, J. F. C., & Cheung, C. C. 2014, ArXiv e-prints, arXiv:1406.4797

Grandi, S. A. 1982, ApJ, 255, 25

Gunn, J. E., Siegmund, W. A., Mannery, E. J., et al. 2006, AJ, 131, 2332

Hooper, E. J., Impey, C. D., Foltz, C. B., & Hewett, P. C. 1995, ApJ, 445, 62

Hopkins, P. F., Strauss, M. A., Hall, P. B., et al. 2004, AJ, 128, 1112

Hubeny, I., Agol, E., Blaes, O., & Krolik, J. H. 2000, ApJ, 533, 710

Jin, C., Ward, M., Done, C., & Gelbord, J. 2012, MNRAS, 420, 1825

Kaspi, S., Smith, P. S., Netzer, H., et al. 2000, ApJ, 533, 631

Koratkar, A., & Blaes, O. 1999, PASP, 111, 1

Kormendy, J., & Ho, L. C. 2013, ARA&A, 51, 511

Kotilainen, J. K., Falomo, R., Decarli, R., et al. 2009, ApJ, 703, 1663

Krawczyk, C. M., Richards, G. T., Gallagher, S. C., et al. 2014, ArXiv e-prints, arXiv:1412.7039

Krolik, J. H. 1999, Active galactic nuclei : from the central black hole to the galactic environment

Kwan, J., & Krolik, J. H. 1981, ApJ, 250, 478

Lagarias, J. C., Reeds, J. A., Wright, M. H., & Wright, P. E. 1998, SIAM Journal on Optimization, 9, 112

Laor, A. 1990, MNRAS, 246, 369

Laor, A., & Davis, S. W. 2014, MNRAS, 438, 3024

Laor, A., & Netzer, H. 1989, MNRAS, 238, 897

Lee, K.-G., Suzuki, N., & Spergel, D. N. 2012, AJ, 143, 51

Li, L.-X., Zimmerman, E. R., Narayan, R., & McClintock, J. E. 2005, ApJS, 157, 335

Malkan, M. A. 1983, ApJ, 268, 582

McLeod, K. K., & Bechtold, J. 2009, ApJ, 704, 415

Miller, L., Peacock, J. A., & Mead, A. R. G. 1990, MNRAS, 244, 207

Mineshige, S., Kawaguchi, T., Takeuchi, M., & Hayashida, K. 2000, PASJ, 52, 499

Netzer, H. 1990, in Active Galactic Nuclei

Netzer, H., Lira, P., Trakhtenbrot, B., Shemmer, O., & Cury, I. 2007, ApJ, 671, 1256

Onken, C. A., Ferrarese, L., Merritt, D., et al. 2004, ApJ, 615, 645

Paczyński, B., & Wiita, P. J. 1980, A&A, 88, 23

Pâris, I., Petitjean, P., Rollinde, E., et al. 2011, A&A, 530, A50

Park, D., Woo, J.-H., Treu, T., et al. 2012, ApJ, 747, 30

Pei, Y. C. 1992, ApJ, 395, 130

Peterson, B. M., Ferrarese, L., Gilbert, K. M., et al. 2004, ApJ, 613, 682

Polletta, M., Tajer, M., Maraschi, L., et al. 2007, ApJ, 663, 81

Popović, L. Č. 2003, ApJ, 599, 140

Rees, M. J. 1984, ARA&A, 22, 471

Richards, G. T., Fan, X., Newberg, H. J., et al. 2002, AJ, 123, 2945

Richards, G. T., Strauss, M. A., Fan, X., et al. 2006, AJ, 131, 2766

Richards, G. T., Kruczek, N. E., Gallagher, S. C., et al. 2011, AJ, 141, 167

Ridgway, S. E., Heckman, T. M., Calzetti, D., & Lehnert, M. 2001, ApJ, 550, 122

Schlegel, D. J., Finkbeiner, D. P., & Davis, M. 1998, ApJ, 500, 525

Schneider, D. P., Richards, G. T., Hall, P. B., et al. 2010, AJ, 139, 2360

Schneider, E. E., Impey, C. D., Trump, J. R., & Salvato, M. 2013, ApJ, 766, 123

Shakura, N. I., & Sunyaev, R. A. 1973, A&A, 24, 337

Shang, Z., Brotherton, M. S., Green, R. F., et al. 2005, ApJ, 619, 41

Shen, Y. 2013, Bulletin of the Astronomical Society of India, 41, 61

Shen, Y., & Liu, X. 2012, ApJ, 753, 125

Shen, Y., Richards, G. T., Strauss, M. A., et al. 2011, ApJS, 194, 45

Shields, G. A. 1978, Nature, 272, 706

Shimura, T., & Takahara, F. 1995, ApJ, 445, 780

Slone, O., & Netzer, H. 2012, MNRAS, 426, 656

Smee, S. A., Gunn, J. E., Uomoto, A., et al. 2013, AJ, 146, 32

Stocke, J. T., Morris, S. L., Weymann, R. J., & Foltz, C. B. 1992, ApJ, 396, 487

Stoughton, C., Lupton, R. H., Bernardi, M., et al. 2002, AJ, 123, 485

Sulentic, J. W., Marziani, P., & Dultzin-Hacyan, D. 2000, ARA&A, 38, 521

Sun, W.-H., & Malkan, M. A. 1989, ApJ, 346, 68

Suzuki, N., Tytler, D., Kirkman, D., O'Meara, J. M., & Lubin, D. 2005, ApJ, 618, 592

Szuszkiewicz, E., Malkan, M. A., & Abramowicz, M. A. 1996, ApJ, 458, 474

Trakhtenbrot, B. 2014, ApJ, 789, L9

Trakhtenbrot, B., & Netzer, H. 2012, MNRAS, 427, 3081

Tsuzuki, Y., Kawara, K., Yoshii, Y., et al. 2006, ApJ, 650, 57

Tytler, D., & Fan, X.-M. 1992, ApJS, 79, 1

Urry, C. M., & Padovani, P. 1995, PASP, 107, 803

Vanden Berk, D. E., Richards, G. T., Bauer, A., et al. 2001, AJ, 122, 549

Vestergaard, M., & Peterson, B. M. 2006, ApJ, 641, 689

Vestergaard, M., & Wilkes, B. J. 2001, ApJS, 134, 1

Wandel, A., Peterson, B. M., & Malkan, M. A. 1999, ApJ, 526, 579

Whiting, M. T., Webster, R. L., & Francis, P. J. 2001, MNRAS, 323, 718

Wilhite, B. C., Brunner, R. J., Schneider, D. P., & Vanden Berk, D. E. 2007, ApJ, 669, 791

Wills, B. J., Netzer, H., & Wills, D. 1985, ApJ, 288, 94

Woo, J.-H., Treu, T., Barth, A. J., et al. 2010, ApJ, 716, 269

Wright, M. H. 1996, in Numerical Analysis 1995

York, D. G., Adelman, J., Anderson, Jr., J. E., et al. 2000, AJ, 120, 1579

This manuscript was prepared with the AAS LaTeX macros v5.2.